Applied Geochemistry 209 (2026) 107048

Contents lists available at ScienceDirect

Applied Geochemistry

journal homepage: www.elsevier.com/locate/apgeochem

Dissolution and surface chemical modifications of mineral fibres in artificial lysosomal fluid

Maria Cristina Di Carlo [a], Paolo Ballirano [a,b], Lorenzo Arrizza [a], Maria Rita Montereali [c], Marzia Fantauzzi [d], Antonella Rossi [d], Giancarlo Capitani [e], Niccolò Magnani [e], Marcello Campione [e], Rossella Yivlialin [f], Gianlorenzo Bussetti [f], Antonella Campopiano [g], Annapaola Cannizzaro [g], Andrea Bloise [h], Fabrizio Bardelli [i], Ida Pettiti [j], Alessandro Pacella [a,*]

[a] Department of Earth Sciences, Sapienza University of Rome, Piazzale Aldo Moro 5, Rome, 00185, Italy
[b] Rectoral Laboratory Fibres and Inorganic Particulate, Sapienza University of Rome, Piazzale Aldo Moro 5, Rome, 00185, Italy
[c] Italian National Agency for New Technologies, ENEA, Casaccia Research Centre, Via Anguillarese 301, Rome, 00123, Italy
[d] INSTM Research Unit, Department of Chemical and Geological Sciences, University of Cagliari, Monserrato, 09042, Italy
[e] Department of Earth & Environmental Sciences, University of Milano - Bicocca, Piazza Della Scienza 4, Milan, 20126, Italy
[f] Department of Physics, Politecnico di Milano, Piazza Leonardo da Vinci 32, Milan, 20133, Italy
[g] Department of Medicine, Epidemiology, Occupational and Environmental Hygiene, INAIL, Via Fontana Candida 1, Rome, 00078, Italy
[h] Department of Biology, Ecology and Earth Sciences, University of Calabria, V. P. Bucci, Arcavacata di Rende, 87036, Italy
[i] National Research Council, Institute of Nanotechnology (CNR-Nanotec), Piazzale Aldo Moro, 5, Rome, 00185, Italy
[j] Department of Chemistry, Sapienza University of Rome, Piazzale Aldo Moro 5, Rome, 00185, Italy

ARTICLE INFO

Editorial handling by: Dr R Coyte

Keywords:
Asbestos
Artificial lysosomal fluid
Fibre dissolution
Surface chemistry
Incongruent dissolution

ABSTRACT

The long-term toxicity of mineral fibres is closely related to their biodurability and surface reactivity, which are in turn strongly influenced by mineral dissolution and surface alteration in lung fluids. We investigated dissolution rates and nanoscale structural, morphological and surface chemical modifications of fibrous antigorite, a non-regulated serpentine polymorph of uncertain pathogenicity, amphibole asbestos (crocidolite and tremolite) and chrysotile, after incubation in artificial lysosomal fluid at pH 4.5, simulating the acidic environment of alveolar macrophages. Fibres were incubated at 37 °C for up to 4 weeks; elemental release was quantified by ICP-OES, and recovered fibres were characterized by PXRD, XPS, FE-SEM, AFM, and TEM. All fibres dissolved incongruently, with preferential leaching of octahedrally coordinated cations and Fe mobilization promoted by citrate complexation. Chrysotile dissolved extensively and became progressively amorphous, consistent with its high specific surface area and preferential removal of Mg from outer octahedral layers. When Si-based dissolution rates are normalised to specific surface area, fibrous antigorite displays biodurability comparable to chrysotile and at least one order of magnitude lower than amphibole asbestos. Among amphiboles, tremolite dissolves more slowly than crocidolite, for which surface erosion exposes underlying Fe(II)-rich layers. Despite the simplified, acellular nature of the ALF model, our results show trends in incongruent dissolution, Fe mobilisation and surface amorphization consistent with *in vivo* toxicological observations. Integration of ALF-based mineralogical and geochemical data with targeted cellular and *in vivo* studies may provide a more robust mechanistic framework for understanding the long-term toxicity of both asbestos and currently unregulated fibrous minerals.

1. Introduction

Asbestos refers to a group of six naturally occurring silicate minerals, comprising chrysotile, which belongs to the serpentine subgroup, and five asbestiform amphibole minerals: tremolite, actinolite, anthophyllite, grunerite (commercially known as amosite), and riebeckite (commercially known as crocidolite). Despite extensive research on asbestos, the precise mechanisms underlying fibre-induced tumour initiation are not fully understood. Current evidence indicates that the pathogenicity of asbestos fibres arises from the combined effects of

* Corresponding author.
E-mail address: alessandro.pacella@uniroma1.it (A. Pacella).

https://doi.org/10.1016/j.apgeochem.2026.107048
Received 17 May 2026; Received in revised form 20 July 2026; Accepted 17 August 2026
Available online 26 August 2026

Table 1
Key features and calculated dissolution rates of the investigated fibrous mineral samples. The number in parentheses is the 1σ uncertainty affecting the last significant digit.

Sample name	Sample locality	Mineral supergroup or subgroup	Crystal-chemical formula	Accessory phases	SSA_{BET} ($m^2\ g^{-1}$)	Reference	Dissolution rate ($\mu mol\ m^{-2}\ h^{-1}$)
Calabrian antigorite	San Mango d'Aquino, Calabria (Italy)	Serpentine	$(Mg_{2.66}Fe^{2+}_{0.10}Fe^{3+}_{0.02}Al_{0.03}Mn_{0.01})_{\Sigma 2.82}(Si_{1.98}Al_{0.02})_{\Sigma 2.00}O_{5.00}(OH)_{3.67}$	Not detected	4.0 (5)	Petriglieri et al. (2025)	1.78 (2)
Ligurian antigorite	Val Varenna, Liguria (Italy)	Serpentine	$(Mg_{2.62}Fe^{2+}_{0.08}Fe^{3+}_{0.04}Al_{0.05}Mn_{0.01})_{\Sigma 2.80}(Si_{1.97}Al_{0.03})_{\Sigma 2.00}O_{5.00}(OH)_{3.65}$	Not detected	5.7 (5)	Petriglieri et al. (2023)	0.864 (3)
UICC Crocidolite	Koegas Mine (South Africa)	Amphibole	$Na_{0.03}Na_{2.00}(Fe^{2+}_{2.21}Fe^{3+}_{2.04}Mg_{0.75})_{\Sigma 5.00}\ (Si_{7.95}Al_{0.02})_{\Sigma 7.97}O_{22}(OH)_2$	Magnetite, quartz, calcite, siderite and minnesotaite (total: 6 wt.%)	8.7 (5)	Pacella et al. (2019)	0.14 (1)
Fibrous tremolite	Iacolinei quarry, Castelluccio Superiore, Basilicata (Italy)	Amphibole	$(Na_{0.04}K_{0.01})_{\Sigma 0.05}(Ca_{1.98}Fe^{2+}_{0.01}Mn_{0.01})_{\Sigma 2.00}(Mg_{4.77}Fe^{2+}_{0.22}Fe^{3+}_{0.01})_{\Sigma 5.00}(Si_{7.98}Al_{0.01})_{\Sigma 7.99}O_{22}(OH)_2$	Chrysotile (3-4 wt.%)	9.2 (5)	Pacella et al. (2024)	0.023 (1)
UICC Chrysotile	Shabani Mine, Zvishavane (Zimbabwe)	Serpentine	$(Mg_{2.81}Fe^{2+}_{0.02}Fe^{3+}_{0.05}Al_{0.06})_{\Sigma 2.94}Si_{2.01}O_{5.00}(OH)_{4.00}$	Magnesite, pyroaurite, calcite and dolomite	27.0 (5)	Petriglieri et al. (2023), 2025	1.03 (2)

physical, chemical, and structural characteristics of fibres, including morphology, biodurability, and surface reactivity (Bonneau et al., 1986a, 1986b; Fubini and Mollo, 1995; Gilmour et al., 1997; Fubini and Areán, 1999; Van Oss et al., 1999; Donaldson et al., 2010; Bernstein et al., 2013). Fibres that are capable of passing through the upper respiratory system and reaching the depth of the lung are "respirable fibres" and, for airborne fibre counting, the World Health Organization (WHO, 1997) defines as fibres "any elongated inorganic particle having length $\geq$ 5 μm, width $\leq$ 3 μm, and length/diameter ratio $\geq$ 3:1". Aerodynamics of this movement are governed mostly by fibre diameter (Gualtieri et al., 2017b). Thanks to their high biodurability, asbestos fibres may reside in lung tissues for decades, significantly increasing the risk of chronic inflammation and carcinogenesis (Donaldson et al., 2010). Moreover, Fe present on fibre surfaces may catalyse the generation of highly reactive hydroxyl radicals ($^{\bullet}OH$), which cannot be enzymatically detoxified and have high potency in damaging biomolecules such as lipids, proteins, or DNA (Shukla et al., 2003; Someah et al., 2023). Specifically, $^{\bullet}OH$ radicals are catalysed by Fe(II) from hydrogen peroxide via the so-called Fenton reaction (Haber and Weiss, 1934; Winterbourn, 1995; Fischbacher et al., 2017). The reaction may also take place in the presence of ferric iron (Fenton-like reaction), that can be reduced to ferrous iron promoting the degradation of another hydrogen peroxide molecule to hydroxyl radical (Turci et al., 2011). It has been demonstrated that the efficiency of $^{\bullet}OH$ yield is dependent on the oxidation state and coordination environment of iron rather than its total content (Andreozzi et al., 2017; Pacella et al., 2018, 2020). Interactions with lung fluids and cells may progressively alter the fibre surface crystal-chemistry and morphology, substantially modify surface properties and thereby influence fibre reactivity and toxicity over time. Therefore, the detailed knowledge of the dissolution mechanisms and surface modifications of mineral fibres in solutions simulating lung fluids is a fundamental prerequisite to understand the fibres' behaviour in the biological environment. Notably, this piece of information may help to shed new light on the mechanisms underlying the observed long-term toxicity of mineral fibres. In this context, the present study investigates the dissolution kinetics and surface chemical–structural modifications of a set of mineral fibres during incubation in artificial lysosomal fluid (ALF, pH 4.5), a standard leaching medium specifically designed to simulate the acidic lysosomal environment of alveolar macrophages, which engulf foreign particles in an attempt to remove them (Innes et al., 2021). Fibrous antigorite, one of the serpentine polymorphs with possible concern for human health and the environment (Cardile et al., 2007; Baumann et al., 2011; Baumann, 2012; Fitzgerald and Harty, 2014; Gazzano et al., 2023; Petriglieri et al., 2023, 2025), was investigated alongside reference amphibole and chrysotile asbestos samples.

Each fibrous sample was incubated in ALF for up to 4 weeks at 37 °C. First, we quantify time-resolved elemental release by inductively coupled plasma optical emission spectroscopy (ICP-OES) to derive Si-based dissolution rates normalised to specific surface area. Second, we elucidate the underlying ALF-induced fibre alteration mechanisms by characterising structural, morphological and surface chemical modifications through a comprehensive multi-analytical approach including powder X-ray diffraction (PXRD), X-ray photoelectron spectroscopy (XPS), field-emission scanning electron microscopy (FE-SEM), atomic force microscopy (AFM) and transmission electron microscopy (TEM). Finally, we critically compare these ALF-based results with published *in vivo* toxicological observations.

2. Materials

2.1. Fibrous samples

In the present study two fibrous antigorite samples were investigated together with two amphibole asbestos samples (crocidolite and fibrous tremolite), and a sample of chrysotile. Table 1 summarises the main

characteristics of the investigated samples, including name, locality, mineral group, crystal-chemical formula, accessory phases, literature references, BET specific surface area (SSA_{BET}), and the surface-normalised dissolution rates determined in this study.

The fibrous antigorite samples were collected from veins within serpentinite bodies of the Gimigliano-Mount Reventino Unit in San Mango d'Aquino (Calabria, Southern Italy) and the Palmaro-Caffarella Unit of the Voltri Massif in Val Varenna (Liguria, North-Eastern Italy). The Calabrian sample, characterized by Petriglieri et al. (2025), has the following crystal-chemical formula: $(Mg_{2.66}Fe^{2+}_{0.10}Fe^{3+}_{0.02}Al_{0.03}Mn_{0.01})_{\Sigma 2.82}(Si_{1.98}Al_{0.02})_{\Sigma 2.00}O_{5.00}(OH)_{3.67}$. Its specific surface area determined with the BET method (SSA_{BET}) is 4.0 (5) $m^2\ g^{-1}$. The Ligurian antigorite, described in Petriglieri et al. (2023), has the crystal-chemical formula $(Mg_{2.62}Fe^{2+}_{0.08}Fe^{3+}_{0.04}Al_{0.05}Mn_{0.01})_{\Sigma 2.80}(Si_{1.97}Al_{0.03})_{\Sigma 2.00}O_{5.00}(OH)_{3.65}$, and a SSA_{BET} of 5.7 (5) $m^2\ g^{-1}$. No accessory phases were detected in either of the two antigorite samples.

The crocidolite sample, that is a fibrous riebeckite supplied by the Union International for Cancer Control (UICC), was collected from the Koegas Mine (South Africa). Its crystal-chemical and structural characterization was conducted by Pacella et al. (2019). The obtained crystal-chemical formula is:

$Na_{0.03}Na_{2.00}(Fe^{2+}_{2.21}Fe^{3+}_{2.04}Mg_{0.75})_{\Sigma 5.00}(Si_{7.95}Al_{0.02})_{\Sigma 7.97}O_{22}(OH)_2$. The SSA_{BET} is 8.7 (5) $m^2\ g^{-1}$. PXRD showed the presence of about 6 wt.% of accessory phases, including magnetite, quartz, calcite, siderite, and minnesotaite.

Fibrous tremolite was sampled from ophiolitic rocks outcropping in the Iacolinei quarry in Castelluccio Superiore (Basilicata, Southern Italy) and was characterized in detail by Pacella et al. (2024). Its crystal-chemical formula is:

$Na_{0.04}K_{0.01})_{\Sigma 0.05}(Ca_{1.98}Fe^{2+}_{0.01}Mn_{0.01})_{\Sigma 2.00}(Mg_{4.77}Fe^{2+}_{0.22}Fe^{3+}_{0.01})_{\Sigma 5.00}(Si_{7.98}Al_{0.01})_{\Sigma 7.99}O_{22}(OH)_2$. The SSA_{BET} is 9.2 (5) $m^2\ g^{-1}$. Minor amounts of chrysotile are present in the sample, as indicated by the weak but detectable 001 reflection at approximately 12° 2θ in the PXRD pattern. The chrysotile content was estimated to be 3–4 wt.% utilizing empirical calibration curves derived from the intensity ratios of the primary diagnostic diffraction reflections of serpentine and amphibole. The relative uncertainty for this quantification method is estimated at ±10%.

The chrysotile sample, also provided by the UICC, was collected from the Shabani asbestos mine in Zvishavane, Zimbabwe. Its crystal-chemical formula is:

$(Mg_{2.81}Fe^{2+}_{0.02}Fe^{3+}_{0.05}Al_{0.06})_{\Sigma 2.94}Si_{2.01}O_{5.00}(OH)_{4.00}$ (Petriglieri et al., 2023, 2025). This sample is characterized by a very high SSA_{BET} of 27.0 (5) $m^2\ g^{-1}$. PXRD identified magnesite, pyroaurite, calcite, and dolomite as accessory phases.

2.2. Reagents for dissolution experiments

The dissolution experiments were conducted in ALF, which was made up following the formulation of Innes et al. (2021). The ALF is the standard solution that simulates the composition and pH of the lysosomal environment within macrophages (Table 2). High-purity reagents were dissolved in ultrapure deionized water (18.2 MΩ cm at 25 °C), produced by a MilliQ Element system (Millipore, France). The pH of the ALF was adjusted at 4.5 by carefully adding NaOH. pH measurements were performed using a portable 250A Orion pH Instrument (Orion Research Inc., Boston, USA) equipped with an Orion gel-filled combination semi-microelectrode (Thermo Electron Corp., Cambridge, England).

3. Experimental

For each experiment, approximately 20 mg of material was suspended in 40 mL of ALF inside polypropylene Falcon™ tubes (BD Falcon™, Corning, Mexico). The tubes were incubated in a thermostatic water-bath set to 37 ± 1 °C placed on a magnetic stirrer and kept under constant agitation using a magnetic stirring bar. Each sample was incubated for 1, 2, 3 and 4 weeks and each dissolution test was performed at least in duplicate. The final 4-week incubation experiments were performed in quintuplicate (n = 5) to recover a sufficient mass of solid residue for multi-technique fibre characterization. A procedural blank sample, consisting of ALF without solid, was made up following the same protocol for each set of experiments. It must be emphasized that, although these conditions do not reproduce the full cellular complexity of the phagolysosomal compartment, they provide a well-defined acidic system that is highly suitable for detecting mineral alterations within a reasonable experimental time. Moreover, Wood et al. (2006) suggested that the phagolysosomal environment within macrophages may behave as at least a partially closed system, so our approach can be considered a geochemical end-member model that captures the key roles of pH, ionic strength and low-molecular-weight ligands (e.g., citrate) on mineral dissolution and surface alteration. The pH was checked after 3 h from the start of the dissolution test and again at the end, confirming its stability throughout the whole experimental time. At the end of each experiment, the solutions were filtered using syringes (BD Plastipack™, Spain) and 0.22 μm GSWP nitrocellulose membrane filters (Millex-HA, Millipore, Ireland). The retained fibres were rinsed with ultrapure water to remove any residual solution, then air-dried prior to the SEM, TEM, AFM, PXRD, and XPS investigations. For antigorite, crocidolite, and tremolite, fibres incubated for 4 weeks were analysed, whereas for chrysotile only the 1-week sample was investigated, as sufficient material could not be recovered after longer incubation times.

4. Methods

4.1. ICP-OES analysis

The filtered solutions were analysed by ICP-OES to quantify the cations released from the fibres. Measurements were performed using a PerkinElmer Optima 2000 DV spectrometer (PerkinElmer, USA) equipped with a cyclonic spray chamber. Prior to analysis, the samples were treated to break down the organic matrix of the ALF solution. Specifically, 5 mL of each filtered solution were mixed with 2.5 mL of 67-69% HNO_3 traceSelect™ Ultra (Honeywell, Fluka, Canada) and 1 mL of 30% H_2O_2 Suprapur® (Merck KGaA, Germany) and then heated up to 100 °C for about 2 h using a DigiBlock mineralization system (LabTech, Italy). After being cooled, MilliQ water was added to the solutions up to the final volume of 10 mL, resulting in a 1:2 dilution. During the analysis, these solutions were further diluted in 1% nitric acid (Ultrapure 60% HNO_3, Merck, Millipore®), resulting in a final dilution of 1:20 or 1:6.

ICP Aristar (BDH) standard solutions in nitric acid for Ca, Mg, Fe, Si, and Al were used to prepare the calibration solutions for ICP-OES analysis. Sodium release could not be quantified because its concentration in the ALF solution exceeds the calibration range (0.05-

Table 2
Composition (g L^{-1}) of the artificial lysosomal fluid (ALF) used for simulation of the acidic conditions of the lysosome.

Compound	Concentration (g L^{-1})
$MgCl_2 \bullet 6H_2O$ (magnesium chloride)	0.106
NaCl (sodium chloride)	3.210
Na_2HPO_4 (disodium hydrogen phosphate)	0.071
Na_2SO_4 (sodium sulphate)	0.039
$CaCl_2 \bullet 2H_2O$ (calcium chloride dihydrate)	0.128
NaOH (sodium hydroxide)	6.000
$C_6H_8O_7$ (citric acid)	20.80
$C_2H_5NO_2$ (glycine)	0.059
$C_6H_5Na_3O_7 \bullet 2H_2O$ (sodium citrate dihydrate)	0.077
$C_4H_4O_6Na_2 \bullet 2H_2O$ (sodium tartrate dihydrate)	0.090
$C_3H_5NaO_3$ (sodium lactate)	0.085
$C_3H_5O_3Na$ (sodium pyruvate)	0.086
pH	**4.5**

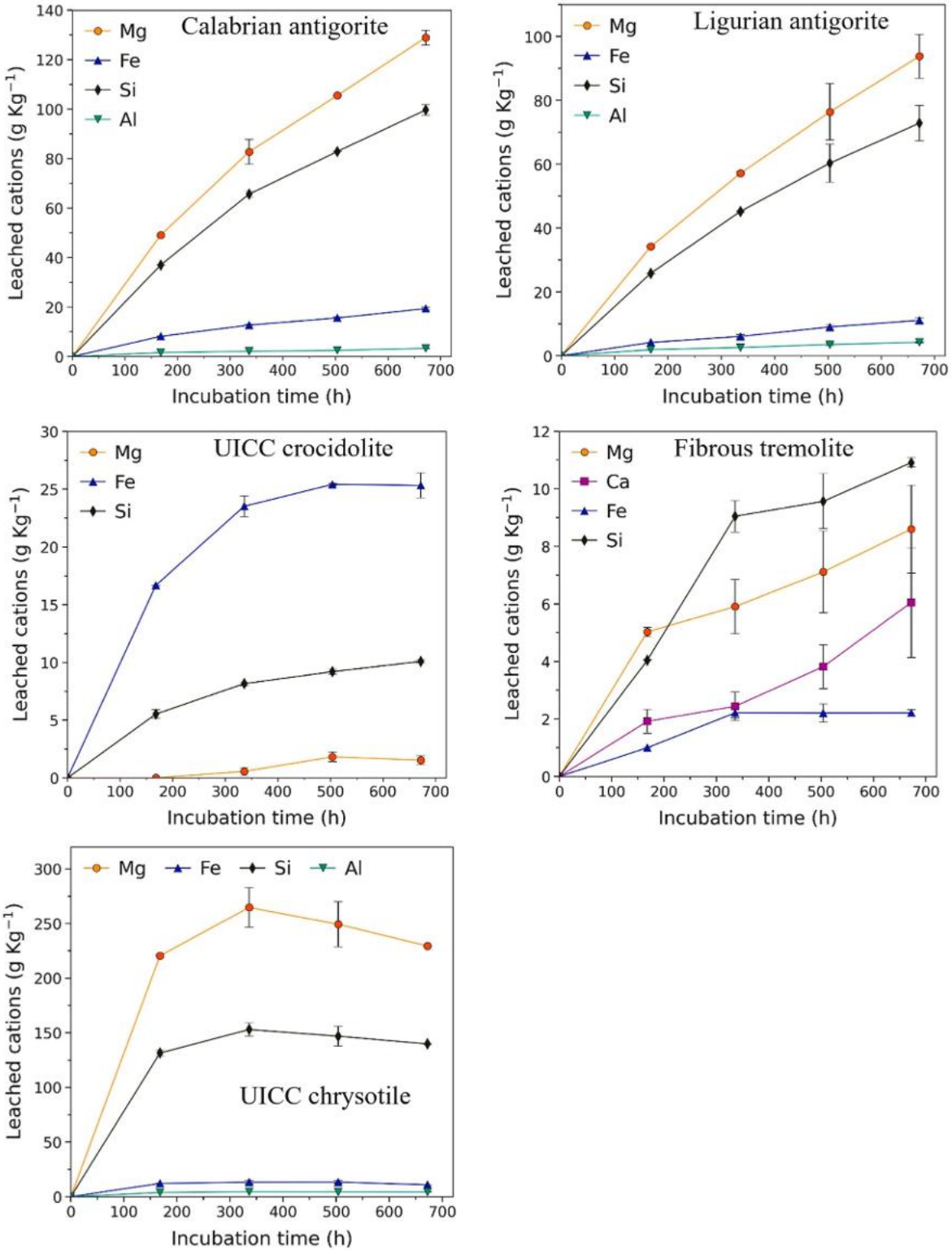

Fig. 1. Dissolution in ALF at pH 4.5 over 0-672 h. Cumulative release of Mg, Fe, Si and Al (g kg^{-1}) determined by ICP-OES for the investigated samples. Error bars represent the min-max range for intermediate data points (n = 2) and the standard deviation for the final 4-week data point (n = 5).

10 mg L^{-1}). The accuracy of the measurements was monitored by periodically reanalysing the standard solutions after each experimental batch.

4.2. PXRD analysis

PXRD data were collected on all five fibrous samples before and after incubation. Measurements were conducted using a Bruker AXS D8 Advance diffractometer (Bruker AXS, Karlsruhe, Germany) operating in θ/θ transmission geometry. The instrument is equipped with incident-

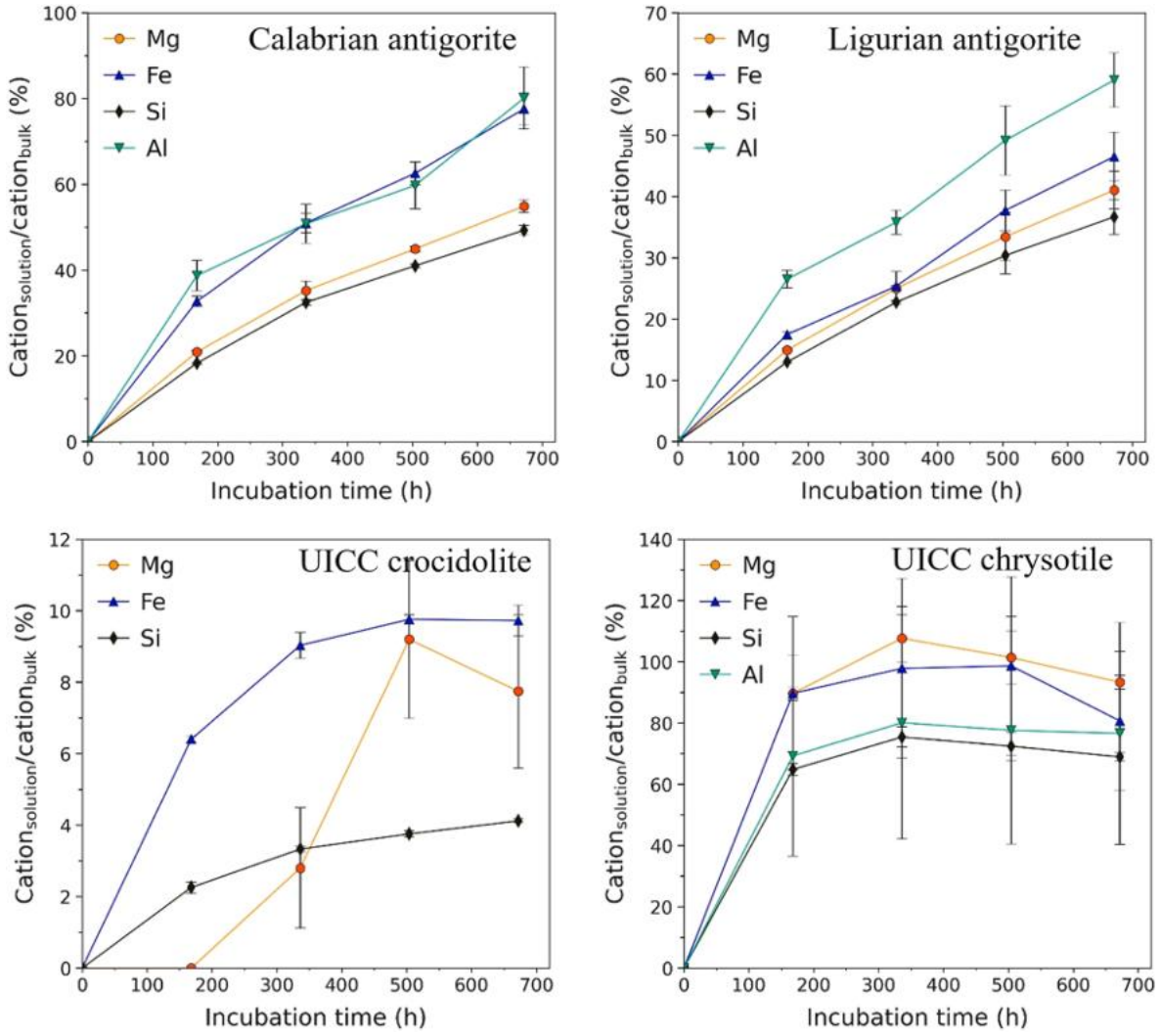

Fig. 2. Fraction of released elements with respect to their amount in the fibre structure for the investigated samples.

beam focusing Göbel mirrors and a position sensitive detector (PSD) VÅntec-1. The samples were gently ground under ethanol in an agate mortar and loaded into borosilicate glass capillaries (0.4 mm diameter). Data were acquired using CuKα radiation in the 5-145° 2θ range, with a step size of 0.0218° 2θ and a counting time of 10 s per step. For each sample, phase identification was performed using the Bruker AXS DIFFRAC. SUITE (Bruker, 2017) software package, integrated with the ICDD PDF-2 Release (ICDD, 2021) database.

4.3. XPS analysis

XPS analyses were carried out to determine the quantitative surface composition and iron speciation of the five fibrous mineral samples after incubation in ALF. Measurements were performed using a Theta Probe spectrometer (Thermo Fisher Scientific, East Grinstead, UK) equipped with a monochromatic Al Kα X-ray source ($h\nu = 1486.6$ eV, 100 W), operating in fixed analyser transmission (FAT) mode. Survey scans were acquired at a pass energy of 200 eV and high-resolution spectra were collected at 100 eV. The nominal spot size was 400 μm, and the base pressure during data acquisition was lower than 10^{-7} Pa. A dual low-energy electron/argon ion flood gun was employed for charge compensation. The emission angle was set at 53° relative to the surface normal. The linearity of the binding energy scale was periodically checked following ISO 15472:2010 standard. Under the adopted experimental conditions the energy resolution, defined as the full width at the half maximum height of Ag $3d_{5/2}$ peak, was 0.9 eV.

The fibres were collected on nitrocellulose membrane filters. All samples were stored under argon atmosphere prior to analysis to minimise post-treatment oxidation. Binding energy values were referenced to the C 1s peak of adventitious carbon set at 285.0 eV. Data were processed using the CasaXPS software package (version 2.3.25PR1.0, Fairley et al., 2021). A Shirley-Sherwood background was applied, and curve fitting was performed using a Gaussian-Lorentzian function. Elemental quantification was based on peak areas corrected, for each element, by the sensitivity factor that takes into account the photoionization cross section (Scofield parameter; Scofield, 1976), the inelastic mean free path calculated according to Seah and Dench (1979), the spectrometer geometry, the asymmetry parameter (Reilman et al., 1976), and the transmission function of the spectrometer, experimentally determined during the calibration procedure (Casula et al., 2025). The estimated uncertainty of atomic percentages is within ±10%.

4.4. FE-SEM analysis

Morphological observations of the fibrous samples were performed using a ZEISS Gemini 500 FE-SEM. Secondary electron images (SEI) were acquired at various magnifications with a working distance of 11 mm, an accelerating voltage of 15 kV and a tilt angle of 0°. Each sample, both pristine and incubated, was mounted on the stub using conductive carbon tape and the surface was covered with a thin

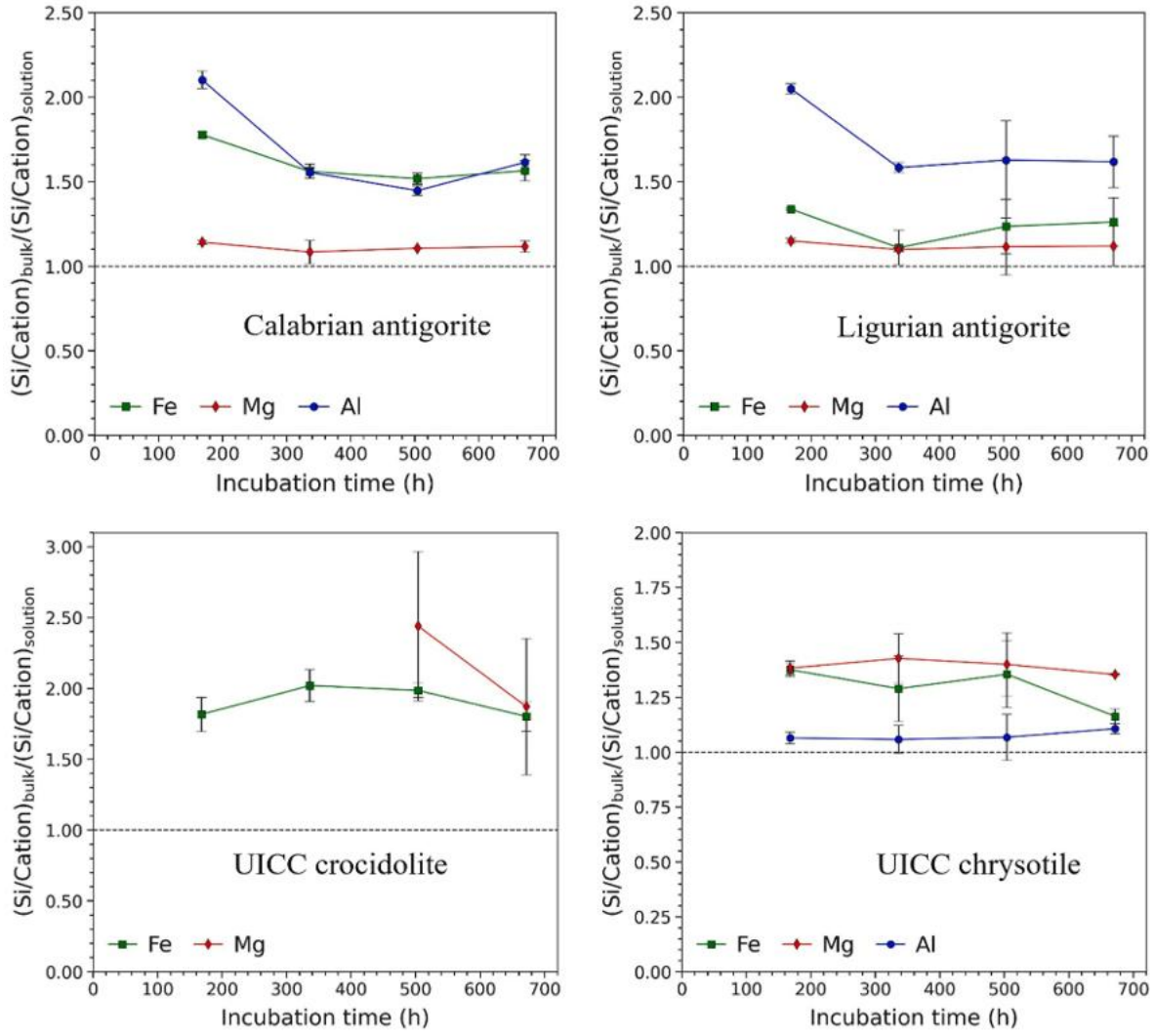

Fig. 3. Variation of the Si/Cation ratio of the released cations (Fe and Mg) at each incubation time compared to that of the pristine sample $(Si/Cation)_{bulk}$ for the investigated samples. The dashed line indicates congruent dissolution.

chromium coating (~5 nm) using a Quorum Q150T ES sputter to make it conductive.

4.5. TEM-EDS analysis

For each sample, pristine fibres and fibres incubated in ALF were dispersed in ethanol (about 1 mm^3 of fibres in 2 mL of solvent) and ultrasonicated for 3 min. Then, ~5 μL of solution was transferred using a pipette onto a 300-mesh copper grid, 3 mm in diameter, supporting a lacey carbon membrane. TEM observations were performed with a JEOL JEM 2100P, equipped with a LaB_6 source and operated at 200 kV. Bright field (BF) and high-resolution electron microscopy (HREM) images and selected area electron diffraction (SAED) patterns were acquired with a 3k × 3k Gatan Rio CMOS Camera. Energy dispersive spectroscopy (EDS) analyses were obtained with an Oxford SSD UltimMax detector holding an 80 mm^2 sensor and windowless design. Analytical data were processed with the Aztec software and HREM images, whenever required, were filtered in the Fourier space using the ABS (average background subtraction) filter as implemented in Digital Micrograph (Gatan) by D.R. G. Mitchell and based on R. Kilaas's work (Kilaas, 1998).

4.6. AFM analysis

Fibres were transferred using a pipette onto a 1 cm × 1 cm plate of native oxide-covered silicon (100) and air-dried. The preparation conditions were analogous to those for TEM-EDS analysis. AFM mapping was performed by using a Keysight 5500 scanning probe microscope. AFM maps were collected in air in tapping mode, using Bruker silicon tips (spring constant of 37 N/m and frequency of 320 kHz). AFM maps were processed with the software WSxM (Horcas et al., 2007). It must be pointed out that for crocidolite and tremolite fibres it was not possible to acquire satisfactory AFM images being the fibres too thin or superficially irregular for AFM tip scan.

4.7. Data treatment and uncertainty notation

Values reported in the form x. xx(y) indicate x. xx ± 0.0y, where the number in parentheses is the 1σ uncertainty affecting the last significant digit, obtained from replicate measurements and/or propagated fitting errors.

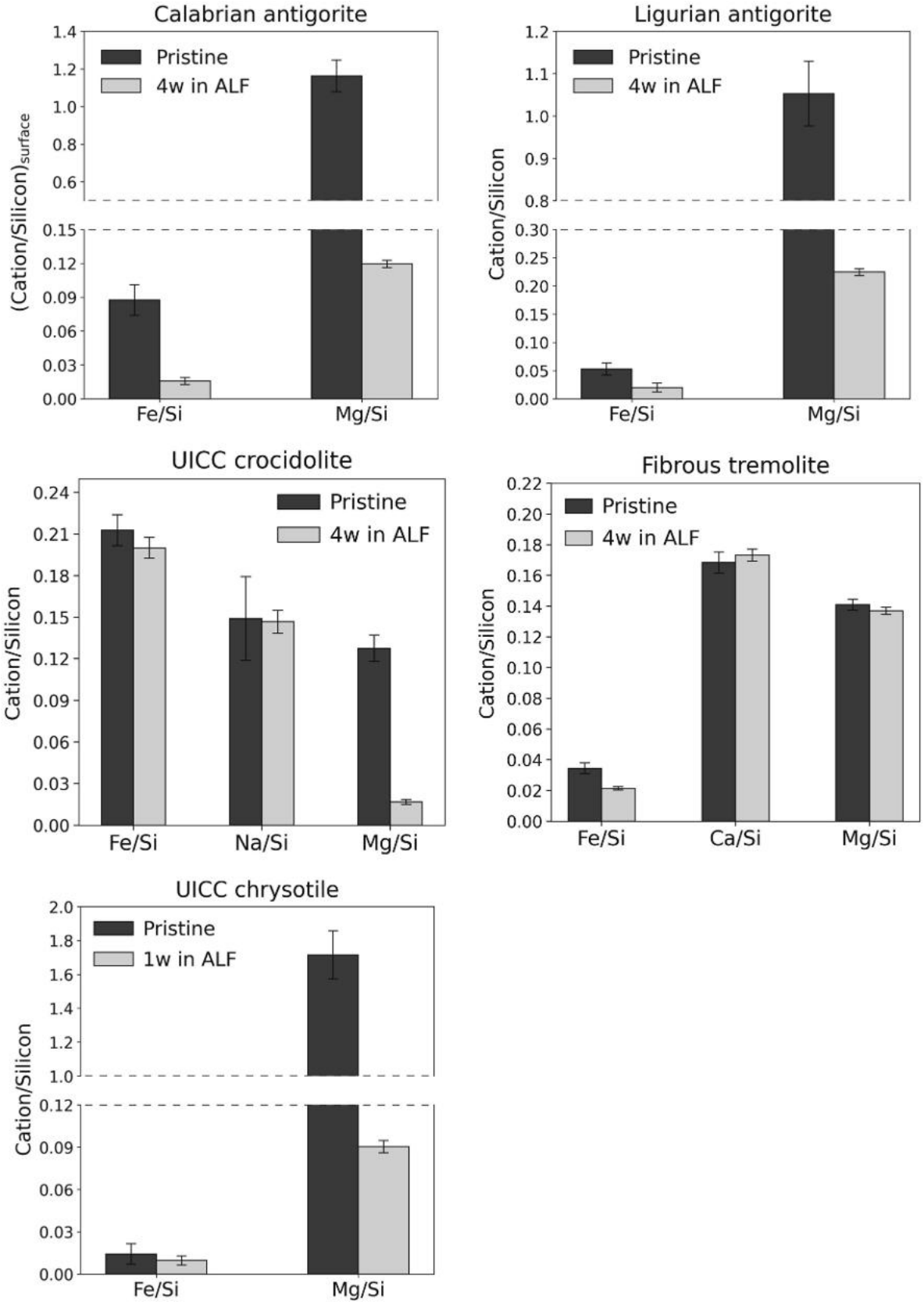

Fig. 4. Cation/silicon ratios (Fe/Si, Mg/Si) at the surface of the investigated fibrous samples before (pristine) and after incubation in ALF at pH 4.5 (1 week = 1w; 4 weeks = 4w). Error bars represent the standard deviation of triplicate measurements.

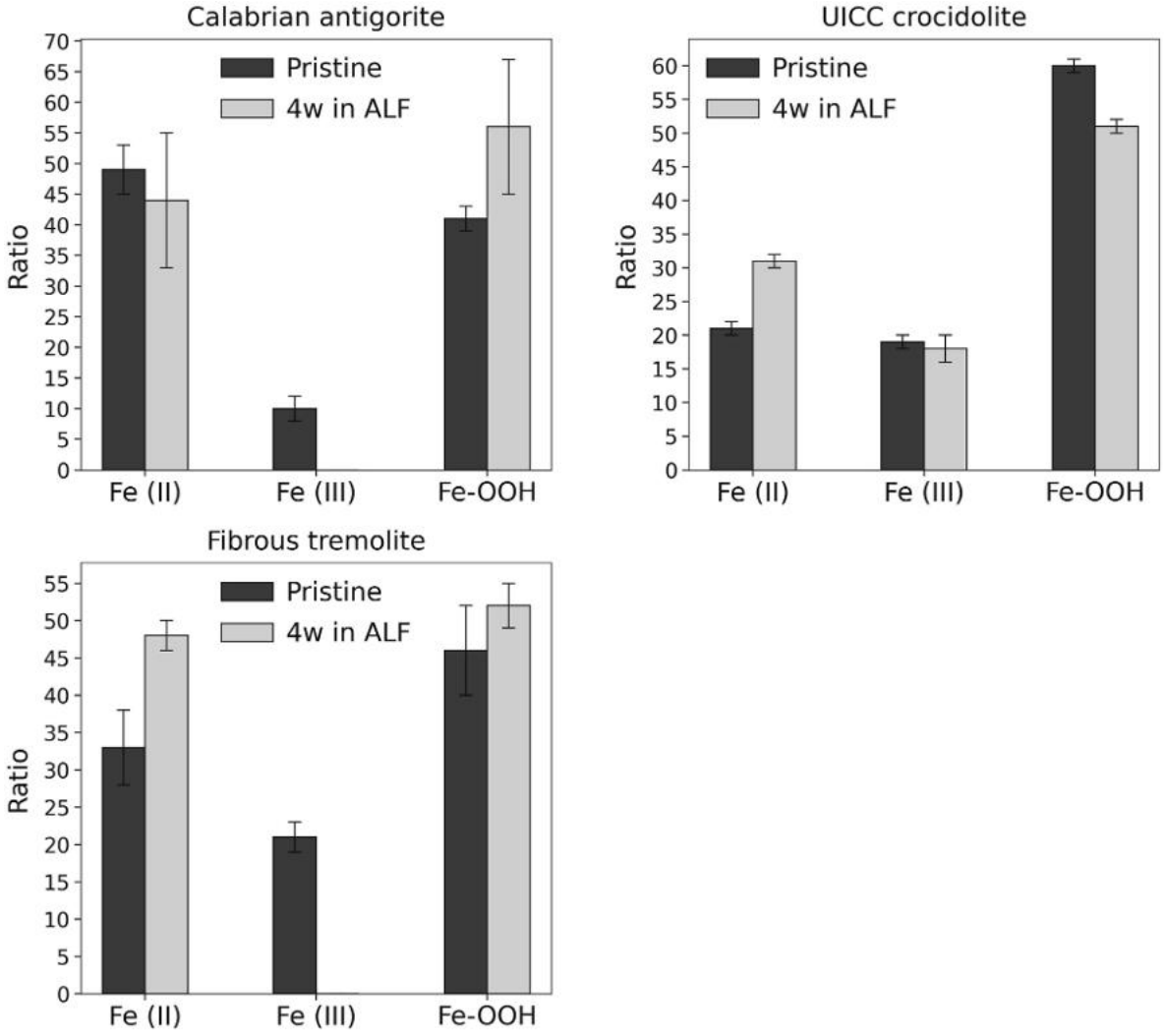

Fig. 5. Relative intensities of Fe $2p_{3/2}$ components [Fe(II), Fe(III), Fe–OOH] before incubation (pristine) and after 4 weeks in ALF at pH 4.5 for the investigated samples. Error bars represent the standard deviation of triplicate measurements.

5. Results and discussion

5.1. Fibrous antigorite

ICP-OES results showed that the two antigorite samples display a similar trend in cation release during incubation in ALF, with concentrations progressively increasing over time. This indicates a continuous fibre dissolution process, approaching but never reaching saturation conditions by the end of the experiment. Mg and Si were the main released elements, whereas Fe and Al were leached out in significantly lower amounts (Fig. 1). However, when considering the actual fractions of the released elements (expressed as a percentage of the leached cation with respect the bulk content), both fibrous antigorite samples show that the fraction of Al and Fe released with respect to their concentration in the fibre structure is very high (up to 80%), even higher than Si and Mg, especially for Calabrian antigorite (Fig. 2). The congruency of the dissolution process was assessed by using the $[(Si/Cation)_{bulk}/(Si/Cation)_{solution}]$ ratio, where molar ratios of Si relative to Mg, Fe, and Al in solution for each sampling time are compared with those obtained for the mineral bulk composition (Fig. 3). For both fibrous antigorite samples, the release of Si and Mg was nearly congruent (i.e., stoichiometric cation release with respect to the bulk composition of the pristine sample), whereas both Fe and Al were preferentially released with respect to Si, especially for the Calabrian sample. It should be noted that the preferential release of these cations is likely enhanced by the efficient chelating action of citrate ions present in the leaching solution (Glusker, 1980). Since Si is generally the rate-determining element in silicate dissolution (Oze and Solt, 2010), it was used for dissolution rate estimation. For the two fibrous antigorite samples, the Si-based dissolution rate was determined by linear regression of Si release over the undersaturation interval (first 2 weeks, i.e., 336 h; Fig. 1). Despite its lower specific surface area, the Calabrian antigorite ($SSA_{BET} = 4.0$ (5) $m^2\ g^{-1}$) exhibits a Si release rate approximately 1.5 times faster than that of the Ligurian sample ($SSA_{BET} = 5.7$ (5) $m^2\ g^{-1}$). Specifically, the calculated SSA-normalised dissolution rates are 1.78 (22) μmol $m^{-2}\ h^{-1}$ and 0.87 (8) μmol $m^{-2}\ h^{-1}$ for the Calabrian and Ligurian antigorite, respectively. This enhanced reactivity in the Calabrian sample is possibly correlated with a lower extent of Al^{3+} substitution for Mg^{2+} within the octahedral sheet, as reflected by the lower $[Al^{3+}/(Mg^{2+} + Al^{3+})]$ ratio of 0.010 compared to 0.017 for the Ligurian specimen. Given that the calculated Madelung site energies for Al–O and Mg–O bonds in octahedral coordination are 0.50 and 0.33, respectively, the Mg–O coordination polyhedra are thermodynamically more susceptible to protonation and subsequent hydrolytic cleavage, thereby accelerating the overall dissolution of the silicate matrix. In addition to chemical features, the possible presence of structural defects was also considered as a potential discriminant factor for the different dissolution rates, as such defects induce strain energy in the crystal, which represents the

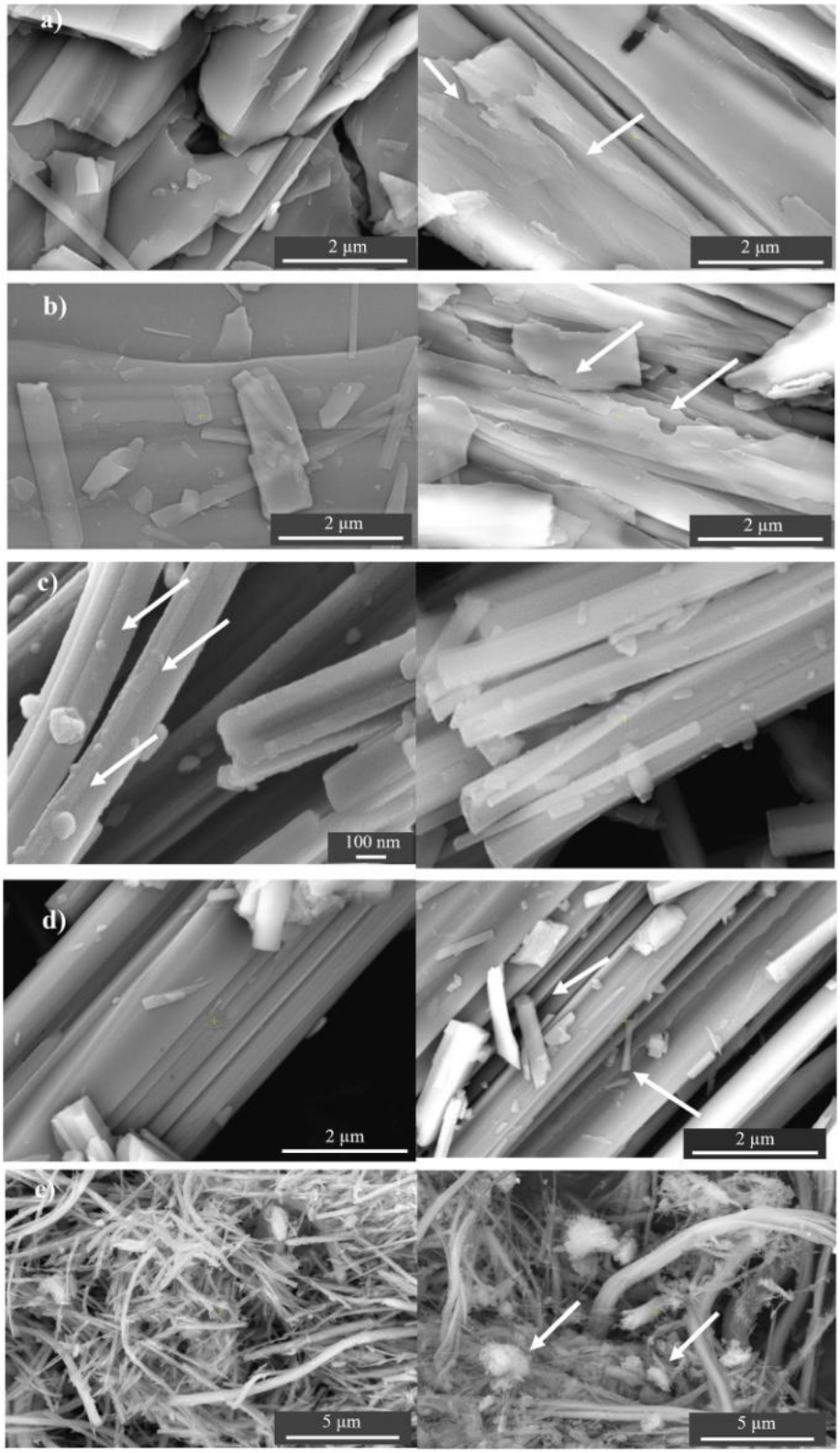

Fig. 6. High-magnification FE-SEM images of fibrous samples before (left) and after 4 weeks in ALF at pH 4.5 (right): (a) Calabrian antigorite, (b) Ligurian antigorite, (c) UICC crocidolite, (d) fibrous tremolite, and (e) UICC chrysotile (after 1 week of incubation in ALF). Arrows show jagged edges and surface erosion (a and b); rounded, bubble-like protuberances and surface nodules distributed along the pristine fibre (c); broken fibre-like particles (d); non-fibrous particles and aggregates (e).

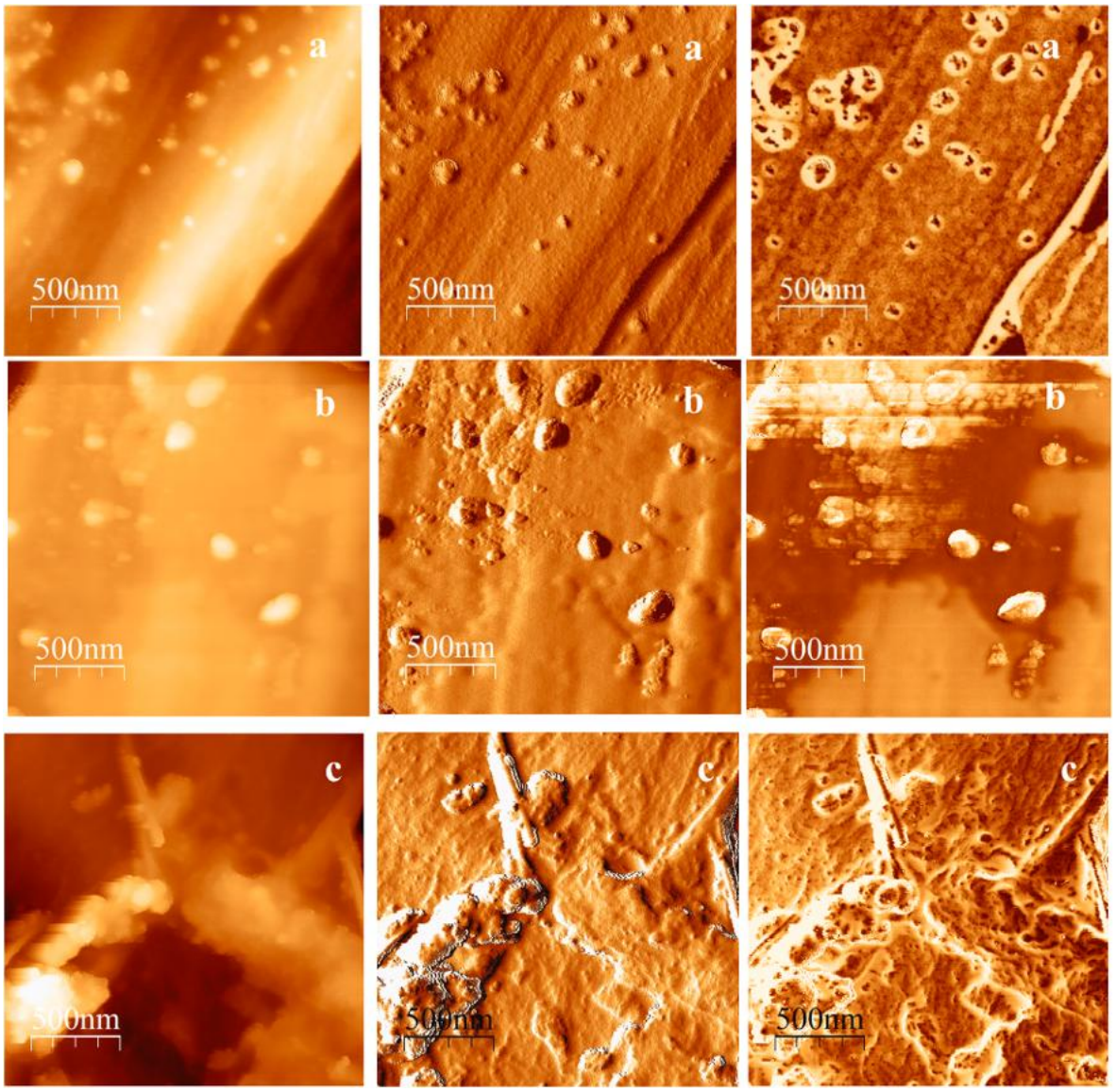

Fig. 7. 2 μm × 2 μm-AFM maps (from left to right: topography, amplitude and phase signals) for sample after incubation in ALF: (a) Calabrian antigorite, (b) Ligurian antigorite, and (c) UICC chrysotile.

energetic driving force for etch pit formation (Lasaga and Lüttge, 2003). However, TEM observations did not reveal any significant difference in terms of defect density between the two samples, which are equally affected by high disorder, therefore suggesting the former chemical mechanism as the prevailing one.

XPS survey spectra showed the presence on antigorite surface of Si, O, Mg, Fe, and small amounts of C, attributable to the adventitious organic contamination layer (Fig. S1). For the Ligurian sample, minor amounts of F are detected on the fibre surface after ALF incubation. Given the absence of fluorine in the pristine sample and the use of PTFE (Teflon)-coated magnetic stir bars, we tentatively attribute this signal to localized degradation of the PTFE coating during prolonged stirring (Amato et al., 2024). In addition, the weak contribution at ~18° 2θ observed in the experimental PXRD patterns is consistent with the presence of PTFE (Fig. S2). This finding provides a reinterpretation of previous observations (Pacella et al., 2021, 2023), where this peak was erroneously assigned to the precipitation of hydrated Mg and Fe sulphates (such as pentahydrate, butlerite, and melanterite). The surface quantitative composition of the incubated fibres was determined from high-resolution XPS spectra by evaluating peak areas and applying sensitivity factors calculated using the first principle method (Fantauzzi et al., 2010). Obtained results indicate substantial surface depletion in Mg and Fe on the surface of both samples after incubation in ALF. In Calabrian antigorite, the Mg/Si ratio decreases from 1.2 (1) to 0.12 (1), and the Fe/Si ratio from 0.087 (14) to 0.016 (4) (Fig. 4). Ligurian antigorite exhibits a similar but less pronounced behaviour, with Mg/Si decreasing from 1.1 (1) to 0.22 (1) and Fe/Si from 0.053 (11) to 0.020 (8) (Fig. 4), in agreement with its lower dissolution rate. It must be pointed out that XPS reveals significant Mg depletion relative to Si at the fibre surface, although the Si/Mg molar ratio in solution measured by ICP was very close to that of the bulk. This apparent discrepancy may result from the rapid dissolution of a sample fraction made of smaller fibres, which can dissolve completely and contribute to the cation concentration into solution with a ratio close to that of the bulk, thereby masking the non-stoichiometric release from bigger, partially leached fibres.

The Fe $2p_{3/2}$ signal was curve-fitted according to the procedure described by Fantauzzi et al. (2010). For the Ligurian sample Fe speciation remained unresolved due to the very low signal-to-noise ratio of the Fe $2p_{3/2}$ signal. In Calabrian antigorite, the Fe signal revealed

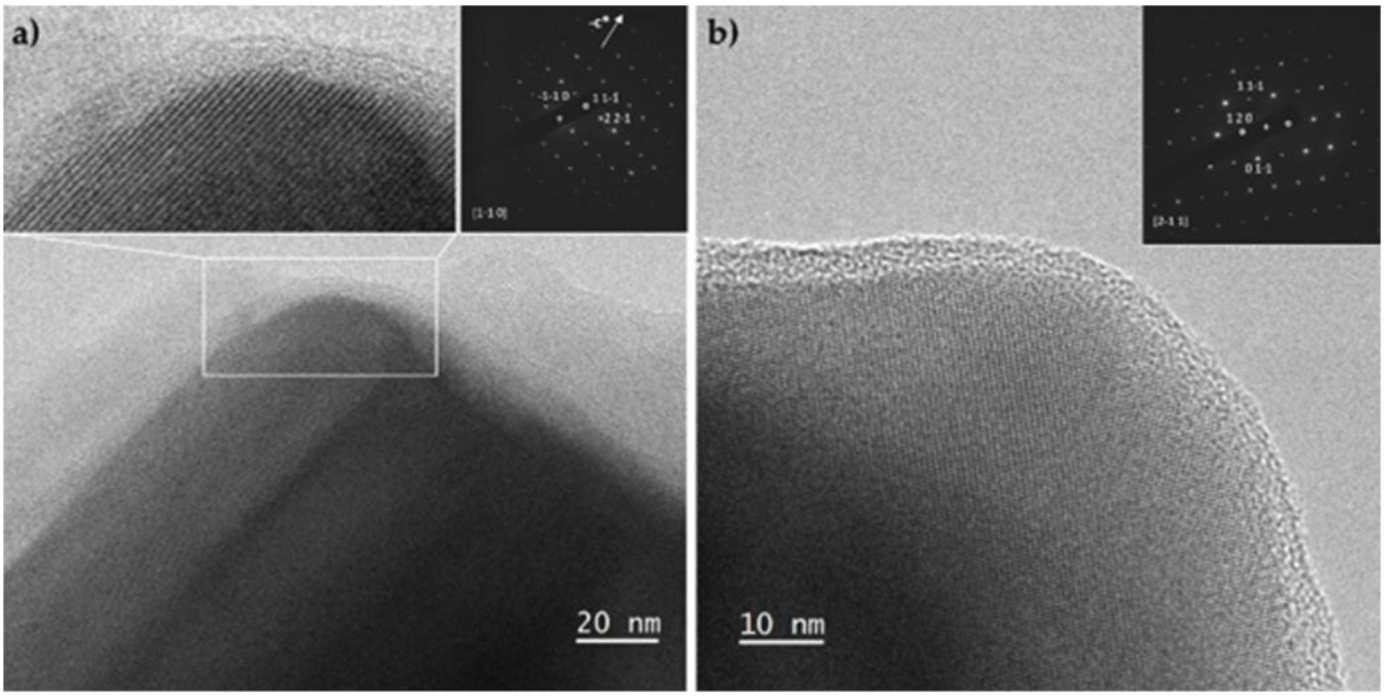

Fig. 8. HRTEM images of (a) UICC crocidolite and (b) fibrous tremolite after 4 weeks of incubation in ALF, with related SAED patterns (shown in the upper-right insets), indexed along [110] and [211], respectively. Note the rounded edges and thin amorphous rims characterizing both amphiboles, suggesting surface dissolution. The diffraction pattern of tremolite could be indexed only with a primitive unit cell, since the $h + k = odd$ reflections should be absent according to the expected $C2/m$ symmetry.

contributions from Fe(II)–O, Fe(III)–O and Fe(III)–OOH components (Fig. S3). The Fe(III)–O component detected in the pristine sample disappeared after 4 weeks of incubation, while Fe(II)–O remained nearly unchanged and Fe(III)–OOH increased from 41% to 56% (Fig. 5). The disappearance of the Fe(III)–O surface species likely results from preferential chelation of Fe(III) over Fe(II) by the citric acid present in ALF, given the higher stability of the Fe(III)–citrate complex compared to Fe(II)–citrate (Königsberger et al., 2000). Nonetheless, this interpretation must be taken with caution due to the low intensity of the Fe signals detected in the sample (Fig. S3).

SEM (Fig. 6a and b) and AFM (Fig. 7a and b) images of ALF-treated fibrous antigorite revealed, for both samples, alteration features such as jagged edges and surface erosion. However, despite these changes, the overall fibrous morphology remained largely preserved. Similar observations were obtained by TEM analysis (Fig. S4). Furthermore, in the AFM maps (Fig. 7a and b), rounded aggregates ranging from tens to hundreds of nanometres are visible on the fibre surface, possibly related to secondary mineralization. In the case of the Calabrian antigorite, such aggregates have a height relative to the fibre surface of 28 (10) nm (number of measurements $n = 49$); the aggregates on the Ligurian antigorite have a height comparable to the Calabrian one, namely 28 (9) nm ($n = 28$).

5.2. UICC crocidolite

ICP-OES results showed that crocidolite released mainly Fe and Si into the ALF solution, reaching maximum concentrations of ca. 25 g kg^{-1} (after 3 weeks or 504 h) and ca. 10 g kg^{-1} (after 4 weeks or 672 h), respectively (Fig. 1). Both elements displayed broadly similar release kinetics, with a steep increase in concentration during the first week (168 h), followed by a progressive decrease in leaching rate and an approach to quasi-steady values after the second week (336 h). It must be pointed out that the dissolution of siderite ($FeCO_3$), occurring as a minor phase in the pristine sample (Table S1), contributed to the total Fe measured in solution, being this phase highly soluble under acidic conditions (Golubev et al., 2009; Pokrovsky et al., 2009). Assuming the complete dissolution of siderite (ca. 1.3 wt.% in the hand sample), approximately 6 g kg^{-1} of Fe can be attributed to this phase, leaving about 19 g kg^{-1} attributable to crocidolite. Mg is released in much lower amounts and becomes substantially detectable only after 3 weeks (504 h) of sample incubation (Fig. 1). When normalised to the fibre bulk composition, Fe is released to a greater extent than Si (Fig. 2) and, as already reported for antigorite, its release is promoted by the chelating action of citric acid present in ALF. However, the fractions of released cations are below 10% of their content in the fibre, indicating a limited overall extent of dissolution.

The congruency of dissolution was evaluated using the same approach adopted for antigorite, by comparing the solution molar ratios of Si relative to Mg and Fe obtained for each sampling time with that of the bulk (retrieved using SEM data from Pacella et al., 2019). The $[(Si/Cation)_{bulk}/(Si/Cation)_{solution}]$ values ranged between 1.80 (10)-2.02(11) for Fe and 1.87(48)-2.44(53) for Mg (Fig. 3), indicating a significant preferential release of these cations with respect to Si (incongruent dissolution). For UICC crocidolite, the Si release rate was calculated from Si concentrations measured over the first week (168 h), corresponding to the undersaturation region, and normalised to the SSA_{BET} [8.7 (5) $m^2\ g^{-1}$], yielding a dissolution rate of 0.14 (1) μmol $m^{-2}\ h^{-1}$.

XPS analyses highlighted a marked decrease in the Mg/Si atomic ratio measured at the fibre surface, from 0.13 (1) in the untreated sample to 0.017 (4) after 4 weeks of incubation in ALF (Fig. 4). Given the low concentrations of accessory phases (Table S1), their contribution to the XPS spectrum (Fig. S1) can be considered negligible. Mg depletion on the fibre surface is in agreement with ICP results and consistent with the lower Madelung site energy of divalent cations hosted in C sites of the amphibole structure compared to the more stable Si tetrahedra chains (Schott and Berner, 1983; Brantley and Chen, 1995). Moreover, although the cations hosted at site $M(4)$ of the amphibole structure are easily leached during amphibole dissolution (Schott and Berner, 1983; Brantley and Chen, 1995; Pacella et al., 2021), the surface Na/Si ratio

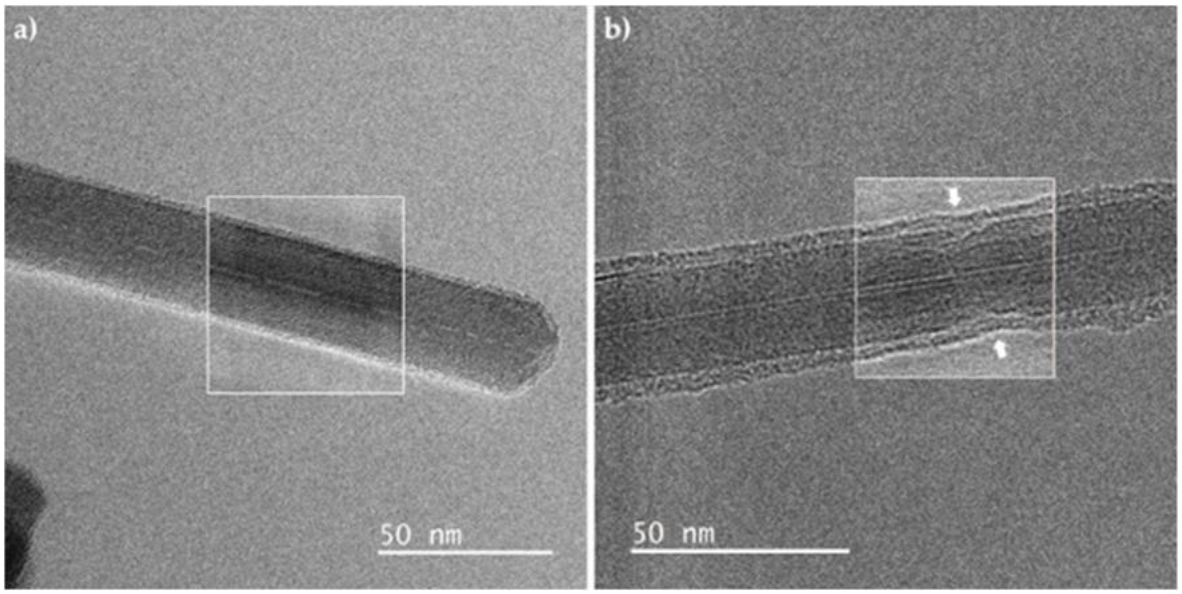

Fig. 9. TEM images showing lattice fringes in UICC chrysotile fibres: (a) pristine sample and (b) sample treated in ALF for 1 week. The central boxes in both images outline the areas filtered in Fourier space to enhance the periodic signal. Both the untreated and ALF-treated samples show a comparable degree of internal crystallinity, but the latter displays more irregular edges with corrosion pits, indicated by arrows.

remains stable (variations within one standard deviation), likely because the release of Na is hindered by its high concentration in the ALF (Table 2). Concerning Fe, the Fe/Si atomic ratio remained constant (Fig. 4), despite significant Fe release evidenced by ICP results (see below for possible explanation).

Results of the Fe $2p_{3/2}$ signal curve-fitting (Fig. S3) show an increase of the Fe(II)–O component from 21% to 31%, while the Fe(III)–O component kept essentially unchanged, and the Fe–OOH signal decreased from 60% to 51% (Fig. 5b). The observed trends in surface Fe speciation are consistent with the results obtained by Pacella et al. (2021) for crocidolite fibres leached in a mimicked Gamble's solution at pH 4.5. These results suggest an erosion of the fibre surface following dissolution, which may promote the occurrence of some portion of the bulk in proximity of (or at) the fibre surface, particularly in the form of Fe(II), of which the bulk is enriched with respect to the oxidized surface. The proposed process is consistent with the unmodified Fe/Si atomic ratio at the fibre surface following dissolution, given the significantly higher Fe content of the bulk compared with that at the surface (ca. 10 at.%. vs ca. 5 at.%., respectively).

The erosion of the silicate framework at the fibre surface is further supported by both FE-SEM (Fig. 6c) and HR-TEM investigation (Fig. 8a), showing that the fibres incubated in ALF up to 4 weeks display smoother, cleaner surfaces (absence of bubble-like features conversely observed on pristine fibres), as well as more rounded edges.

5.3. Fibrous tremolite (Castelluccio Superiore)

ICP-OES data for fibrous tremolite (Fig. 1) are strongly affected by the selective dissolution of accessory chrysotile (estimated to be 3–4 wt. % in the starting material). The PXRD pattern of the ALF-treated sample (Fig. S5) confirms that chrysotile completely dissolves under these acidic conditions. Consequently, neither the fraction of leached cations relative to the tremolite stoichiometry nor the resulting Si/cation ratios in solution could be reliably quantified, and ICP-OES results are thus excluded from detailed discussion. However, given that chrysotile undergoes near-complete dissolution in ALF within two weeks (see Section 5.3), the Si dissolution rate for tremolite fibres, normalised to the sample BET surface area, was tentatively estimated from the Si release over the undersaturation interval (first 2 weeks, i.e., 336 h). This was achieved after subtracting the Si contribution attributable to the serpentine phase, which corresponds to approximately 7 g kg^{-1} of dissolved Si. The calculated dissolution rate is 0.023 (1) μmol m^{-2} h^{-1}, approximately six times lower than that of UICC crocidolite fibres [0.14 (1) μmol m^{-2} h^{-1}]. This outcome is in excellent agreement with previous findings by Pacella et al. (2021) obtained using a modified Gamble's solution at pH 4.5.

The quantitative surface composition, determined from XPS high-resolution spectra, remains almost unchanged compared to the chemical composition of the pristine surface (differences are within two standard deviations, Fig. 4), in agreement with the low dissolution rate of tremolite fibres. It must be pointed out that, due to the small amount of chrysotile in the hand sample (below 5 wt. %), its contribution to the XPS data of the pristine sample may be considered negligible.

Fe $2p_{3/2}$ peak curve fitting (Fig. S3) revealed the disappearance of the Fe(III)–O component, while the Fe(II)–O component increased from 33% to 48% (Fig. 5). Although this result may be affected by the low signal-to-noise ratio, the disappearance of the Fe(III) component is consistent with the preferential complexation of surface Fe(III) by citric acid, in line with the higher stability constant of Fe(III)–citrate compared with Fe(II)–citrate (Königsberger et al., 2000).

As observed by FE-SEM images (Fig. 6d), the tremolite fibres from Castelluccio Superiore after 4 weeks of incubation in ALF appear to contain more broken fibre-like particles, although the sample retain its typical fibrous morphology, characterized by long, rigid fibres arranged in bundles, with minor presence of significant signs of surface erosion and jagged edges. Besides, when examined in detail by TEM, ALF-treated tremolite fibres display amorphous regions along the edges that can be interpreted as evidence of surface dissolution (Fig. 8b).

5.4. UICC chrysotile

ICP-OES measurements indicated that Mg was the most abundant cation released during UICC chrysotile dissolution, followed by Si, Fe, and Al (Fig. 1). Cation concentrations sharply increased during the first week (168 h) of incubation in ALF, reaching maximum values after 14 days, and subsequently remained approximately constant until the end of the experiment (Fig. 1). Normalisation to the bulk fibre composition (Fig. 2) highlighted a released fraction of approximately 70% for Si and 80% for Al, whereas Mg and Fe were almost completely leached from the mineral structure. It must be noted that the total measured release of Mg and Fe includes a minor contribution from highly soluble accessory

minerals (magnesite, dolomite, and pyroaurite) detected by PXRD in the bulk sample (Table S2), though this does not alter the overall trend observed for the chrysotile fibres (see the following discussion). This extreme leaching behaviour reflects the crystal structure of chrysotile, which consists of rolled-up tetrahedral-octahedral sheets assembled into cylindrical fibrils. Because Mg occupies the octahedral sites preferentially exposed on the outermost surface, it is readily leached under acidic conditions, thereby destabilising the structure and promoting the delamination and fragmentation of the residual silicate sheets (Gualtieri et al., 2018, 2019). Accordingly, the $[(Si/Cation)_{bulk}/(Si/Cation)_{solution}]$ ratio remained consistently above 1 throughout the entire experimental timeframe for both Mg and Fe, confirming the strongly incongruent nature of the dissolution process (Fig. 3). Notably, this mechanism led to the complete structural breakdown of most fibres within just two weeks of incubation in ALF. The Si dissolution rate was calculated from the amount of Si released over the first week (168 h), corresponding to the undersaturation region, and then normalised to the sample SSA_{BET} (ca. 27 $m^2 g^{-1}$). The resulting rate is 1.03 (2) μmol m^{-2} h^{-1}. Based on equivalent surface area, chrysotile fibres release Si approximately one order of magnitude faster than crocidolite fibres [0.14 (1) μmol m^{-2} h^{-1}]. It must be pointed out that, during mineral dissolution, the specific surface area may evolve with time, and the overall dissolution rate may have intrinsic variability (Gautier et al., 2001; Lüttge et al., 2013). Regarding our dissolution rate estimation, the PXRD patterns revealed that significant weakening and broadening of the characteristic diffraction peaks were already evident after 1 week of incubation in ALF and became even more pronounced after 4 weeks, indicating extensive amorphization (Fig. S6). On this basis, the Si release for chrysotile is expected to be inherently variable *in vivo* during fibre clearance by macrophages, owing to significant modifications in the density distribution of reactive sites on the dissolving surface.

Due to the very rapid dissolution of chrysotile, XPS analysis could only be performed on the sample incubated for 1 week (Fig. S1), as only a very small amount of material was recovered after longer incubation times. On this basis, direct comparison of surface depletion and alteration among chrysotile, fibrous antigorite and amphibole asbestos must be interpreted with caution. Nevertheless, significant depletion of surface Mg relative to the pristine sample is already evident after 1 week (168 h) of fibre incubation, as the Mg/Si atomic ratio markedly decreased from 1.7 (1) in the pristine sample to 0.090 (5) in the ALF-incubated sample (Fig. 3). As already mentioned for antigorite fibres, the preferential leaching of Mg reflects the lower bond strength of this cation in the octahedral layers of the serpentine structure, compared with the stronger Si–O bond (Lacinska et al., 2016). It must be pointed out that the deviation from bulk stoichiometry highlighted by XPS is much more marked than that inferred in solution from ICP data. This discrepancy may be attributed to the rapid and complete dissolution of a significant fraction of the chrysotile fibres already after 1 week of sample incubation, resulting in a cation stoichiometry in solution very close to that of the bulk. Due to the very low signal-to-noise ratio of the Fe $2p_{3/2}$ peak, iron speciation could not be determined for this sample, despite the large number of acquisition scans.

SEM images show that the characteristic curled fibrous morphology of chrysotile is largely preserved in the residual fibres after 1 week of dissolution (Fig. 6e). Notably, several studies, both *in vitro* and *in vivo*, indicate that chrysotile undergoes pseudomorphic amorphization, yielding a silica-rich residue that preserves the original fibrous morphology (Pollastri et al., 2016; Gualtieri et al., 2017a, 2018). TEM observations allow a further refinement of this mechanism, showing that after 1 week of incubation, and thus dissolution, amorphization affects the external regions of the fibres, whereas the fibre interior retains a crystallinity comparable to that of pristine fibres (Fig. 9). Moreover, non-fibrous particles and aggregates, absent in the pristine sample and possibly related to secondary mineralization, are observed in the ALF-treated sample by SEM (Fig. 6e). Accordingly, AFM maps show the presence of these aggregates along with some smaller fibres (Fig. 7c). The height of the roundish aggregates is 184 (86) nm (n = 10).

5.5. Implications for in vivo observations and long-term toxicity

Chronic inhalation bioassays and pathological investigations have shown that chrysotile exhibits a comparatively short residence time in the lung, undergoing progressive chemical and structural degradation and relatively rapid clearance, whereas amphibole asbestos (e.g., crocidolite, amosite, tremolite) are markedly more durable and accumulate over time in lung and pleural tissues (Wagner et al., 1982; Bernstein et al., 2003, 2021; Donaldson et al., 2010; Gualtieri et al., 2017b). Although biodurability should not be considered synonymous of biopersistence, our ALF experiments reproduced this hierarchy when dissolution rates were calculated accounting for differences in BET surface area, mineral molar mass (912 g mol^{-1} and 278 g mol^{-1} for crocidolite and chrysotile, respectively), and stoichiometry (crocidolite contains 8 mols of Si per mol of mineral, compared with 2 mols for chrysotile): chrysotile dissolves at rate approximately thirty times higher than amphibole asbestos, leading to extensive fibre surface alteration and almost complete physical destruction of the fibres within weeks to months. The incongruent dissolution documented here—characterised by preferential leaching of octahedrally coordinated Mg relative to Si and by the development of silica-enriched alteration rims on chrysotile—closely mirrors *in vivo* observations, where fibres recovered from animal lungs or human tissues are heavily depleted in Mg, structurally weakened and frequently transformed into pseudomorphic, silica-rich residues that preserve the fibrous morphology but have lost their internal crystallinity (Churg et al., 1993; Bernstein et al., 2003; Pollastri et al., 2016; Gualtieri et al., 2017a). Conversely, the low dissolution rates, limited amorphization and preservation of long, rigid morphologies for crocidolite and tremolite in ALF are in line with the extreme *in vivo* biopersisitence of amphibole asbestos documented in rodent inhalation studies and human autopsy series, where amphibole fibres are often found essentially intact decades after exposure and are strongly associated with mesothelioma and lung cancer (Wagner et al., 1982; Bernstein et al., 2008; Donaldson et al., 2010). The composition of ALF, and particularly the presence of citric acid, reflects key aspects of the phagolysosomal environment, where macrophages deploy low molecular weight chelators and Fe binding biomolecules to dissolve inhaled particles (Gulumian et al., 2001). Accordingly, our combined ICP-OES and XPS results showed that under the adopted experimental conditions Fe is efficiently mobilised via citrate complexation, providing a plausible analogue of iron mobilisation and rearrangement on fibre surfaces within phagolysosomes *in vivo* (Nagai et al., 2011). The persistence of catalytically active Fe sites at, or near, the fibre surface is critical because Fe(II) and Fe(III) in suitable coordination environments drive Fenton and Fenton-like reactions generating highly reactive hydroxyl radicals ($^{\bullet}OH$) from hydrogen peroxide (Haber and Weiss, 1934; Shukla et al., 2003; Turci et al., 2011; Fischbacher et al., 2017; Ghio et al., 2023). Toxicological and clinical studies have repeatedly linked oxidative stress, DNA damage and chronic inflammation to redox-active iron associated with asbestos surface (Fubini and Mollo, 1995; Gilmour et al., 1997; Someah et al., 2023). In this way, the amphibole structure could act as a durable framework that may sustain long-term oxidative potential, whereas rapidly dissolving chrysotile may tend to lose reactivity as fibres are cleared. Notably, crocidolite may exhibit enhanced efficacy in generating hydroxyl radicals ($^{\bullet}OH$) via the Fenton mechanism despite the concurrent Fe leaching induced by citric acid or other biological chelators, owing to the continuous exposure of reactive Fe(II) surface sites during fibre alteration.

6. Conclusions

The present study details the dissolution kinetics and surface modifications of selected serpentine (chrysotile and fibrous antigorite) and

amphibole (crocidolite and tremolite) mineral fibres during a 4-week exposure to a simulated lysosomal environment (ALF, pH 4.5). ALF is the standard solution designed to mimic the lysosomal environment in macrophages, specialized immune cells capable of engulfing and digesting fibres once inhaled. All investigated fibres undergo incongruent dissolution in ALF, with preferential loss of octahedrally coordinated cations and citrate-promoted Fe and Al mobilization; when normalised to specific surface area, serpentines (chrysotile and fibrous antigorite) show Si-based dissolution rates much higher than amphibole asbestos (crocidolite, tremolite). Chrysotile undergoes rapid preferential removal of Mg from outer octahedral layers and surface amorphization, leading to near-complete fibre decomposition on a timescale of weeks to months, consistent with its lower *in vivo* residence time. The two fibrous antigorite samples displayed comparable dissolution rates, although the Calabrian sample dissolved slightly faster than the Ligurian one. This difference is most likely related to its lower aluminium content (Mellini, 1982; Lacinska et al., 2016), rather than to variations in structural defect density, as supported by TEM observations. Despite similar morphology under TEM, tremolite fibres exhibited a lower Si dissolution rate than UICC crocidolite, in line with previous works (Pacella et al., 2021, 2023) and with crystal-chemical controls indicating greater solubility of Fe-rich amphiboles versus Fe-poor analogues (Siever and Woodford, 1979). UICC crocidolite dissolution produced surface erosion and progressive exposure of Fe(II)-rich subsurface layers, a surface chemical evolution that is likely to modulate long-term oxidative potential. Although our results are constrained by the simplifications of the acellular ALF model, they show internally coherent trends in incongruent dissolution, Fe mobilisation and surface amorphization that are in line with *in vivo* toxicological data. Therefore, integration of ALF-based mineralogical and geochemical data with targeted cellular and *in vivo* studies may provide a more robust mechanistic framework to gain new insights into the processes underlying the long-term toxicity of asbestos and currently unregulated fibrous minerals such as antigorite.

CRediT authorship contribution statement

Maria Cristina Di Carlo: Writing – review & editing, Writing – original draft, Supervision, Methodology, Investigation. **Paolo Ballirano:** Writing – review & editing, Writing – original draft, Methodology, Investigation. **Lorenzo Arrizza:** Writing – review & editing, Writing – original draft, Methodology, Investigation. **Maria Rita Montereali:** Writing – review & editing, Writing – original draft, Methodology, Investigation. **Marzia Fantauzzi:** Writing – review & editing, Writing – original draft, Methodology, Investigation. **Antonella Rossi:** Writing – review & editing, Writing – original draft, Methodology, Investigation. **Giancarlo Capitani:** Writing – review & editing, Writing – original draft, Methodology, Investigation. **Niccolò Magnani:** Writing – review & editing, Writing – original draft, Methodology, Investigation. **Marcello Campione:** Writing – review & editing, Writing – original draft, Methodology, Investigation. **Rossella Yivlialin:** Writing – review & editing, Writing – original draft, Methodology, Investigation. **Gianlorenzo Bussetti:** Writing – review & editing, Writing – original draft, Methodology, Investigation. **Antonella Campopiano:** Writing – review & editing, Writing – original draft, Methodology, Investigation. **Annapaola Cannizzaro:** Writing – review & editing, Writing – original draft, Methodology, Investigation. **Andrea Bloise:** Writing – review & editing, Writing – original draft, Methodology, Investigation. **Fabrizio Bardelli:** Writing – review & editing, Writing – original draft, Methodology, Investigation. **Ida Pettiti:** Writing – review & editing, Writing – original draft, Methodology, Investigation. **Alessandro Pacella:** Writing – review & editing, Writing – original draft, Supervision, Project administration, Methodology, Investigation, Funding acquisition, Conceptualization.

Declaration of competing interest

The authors declare the following financial interests/personal relationships which may be considered as potential competing interests: Alessandro Pacella reports financial support was provided by University of Rome La Sapienza. All authors declare that they have no known competing financial interests or personal relationships that could have appeared to influence the work reported in this paper.

Acknowledgements

This project is funded by the INAIL - BRIC 2022 project (grant number ID 67; CUP: B87G23000090005).

TEM observations were performed at the Platform of Microscopy of the University of Milano-Bicocca (PMiB, https://piattaformadimicroscopia.unimib.it/).

The AFM measurements were performed at the Solid-LiquidInterface Nanomicroscopy and Spectroscopy laboratory (SoLINano-Σ LAB, https://www.polimi.it/en/research/laboratories/interdepartmental-laboratories/solinano-s-lab-solid-liquid-interface-nanomicroscopy-and-spectroscopy-lab) which is an interdepartmental facility at Politecnico di Milano.

Appendix A. Supplementary data

Supplementary data to this article can be found online at https://doi.org/10.1016/j.apgeochem.2026.107048.

Data availability

Data will be made available on request.

References

Amato, P., Fantauzzi, M., Bifulco, A., Imparato, C., Rossi, A., Aronne, A., Sannino, F., 2024. Physical and chemical degradation of PTFE magnetic stir bars induced by TiO2-based materials. Appl. Surf. Sci. 676, 161018. https://doi.org/10.1016/j.apsusc.2024.161018.

Andreozzi, G.B., Pacella, A., Corazzari, I., Tomatis, M., Turci, F., 2017. Surface reactivity of amphibole asbestos: a comparison between crocidolite and tremolite. Sci. Rep. 7, 14696. https://doi.org/10.1038/s41598-017-14480-z.

Baumann, F., 2012. Environmental exposure to carcinogenic fibers due to serpentinite paved roads in New Caledonia: lessons in environmental epidemiology and in prevention. In: Geological Society of America, Cordilleran Section, 108th Annual Meeting, Abstracts with Programs.

Baumann, F., Maurizot, P., Mangeas, M., Ambrosi, J.-P., Douwes, J., Robineau, B., 2011. Pleural mesothelioma in New Caledonia: associations with environmental risk factors. Environ. Health Perspect. 119, 695–700. https://doi.org/10.1289/ehp.1002862.

Bernstein, D.M., Chevalier, J., Smith, P., 2003. Comparison of Calidria chrysotile asbestos to pure tremolite: inhalation biopersistence and histopathology following short-term exposure. Inhal. Toxicol. 15, 1387–1419. https://doi.org/10.1080/08958370304434.

Bernstein, D.M., Dunnigan, J., Hesterberg, T., Brown, R., Velasco, J.A.L., Barrera, R., Hoskins, J., Gibbs, A., 2013. Health risk of chrysotile revisited. Crit. Rev. Toxicol. 43, 154–183. https://doi.org/10.3109/10408444.2012.756454.

Bernstein, D.M., Rogers, R., Sepulveda, R., Donaldson, K., Schuler, D., Gaering, S., Kunzendorf, P., Chevalier, J., Holm, S.E., 2008. The pathological response and fate in the lung and pleura of chrysotile in combination with fine particles compared to amosite asbestos following short term inhalation exposure: interim results. Inhal. Toxicol. 20, 1023–1045. https://doi.org/10.1080/08958370802105495.

Bernstein, D.M., Toth, B., Rogers, R.A., Kunzendorf, P., Phillips, J.I., Schaudien, D., 2021. Final results from a 90-day quantitative inhalation toxicology study evaluating the dose-response and fate in the lung and pleura of chrysotile-containing brake dust compared to TiO2, chrysotile, crocidolite or amosite asbestos: histopathological examination, confocal microscopy and collagen quantification of the lung and pleural cavity. Toxicol. Appl. Pharmacol. 424, 115598. https://doi.org/10.1016/j.taap.2021.115598.

Bonneau, L., Malard, C., Pezerat, H., 1986a. Studies on surface properties of asbestos: II. Role of dimensional characteristics and surface properties of mineral fibers in the induction of pleural tumors. Environ. Res. 41, 268–275. https://doi.org/10.1016/S0013-9351(86)80188-8.

Bonneau, L., Suquet, H., Malard, C., Pezerat, H., 1986b. Studies on surface properties of asbestos: I. Active sites on surface of chrysotile and amphiboles. Environ. Res. 41, 251–267. https://doi.org/10.1016/S0013-9351(86)80187-6.

Brantley, S.L., Chen, Y., 1995. Chemical weathering rates of pyroxenes and amphiboles. In: White, A.F., Brantley, Susan L. (Eds.), Chemical Weathering Rates of Silicate Minerals. De Gruyter, pp. 119–172.
Bruker, A.X.S., 2017. DIFFRAC.SUITE. Bruker AXS GmbH, Karlsruhe, Germany.
Cardile, V., Lombardo, L., Belluso, E., Panico, A., Capella, S., Balazy, M., 2007. Toxicity and carcinogenicity mechanisms of fibrous antigorite. Int. J. Environ. Res. Publ. Health 4, 1–9. https://doi.org/10.3390/ijerph2007010001.
Casula, G., Biggio, D., Elsener, B., Rossi, A., Fantauzzi, M., 2025. XPS spectra of chitosan powder and film acquired by monochromatic Al Kα X-ray source. Surf. Sci. Spectra 32, 024008. https://doi.org/10.1116/6.0004760.
Churg, A., Wiggs, B., Depaoli, L., Kampe, B., Stevens, B., 1993. Mineralogic analysis of the lungs of urban dwellers and workers with mesothelioma in Vancouver, Canada. Am. Rev. Respir. Dis. 147, 454–460. https://doi.org/10.1164/ajrccm/147.2.454.
Donaldson, K., Murphy, F.A., Duffin, R., Poland, C.A., 2010. Asbestos, carbon nanotubes and the pleural mesothelium: a review of the hypothesis regarding the role of long fibre retention in the parietal pleura, inflammation and mesothelioma. Part. Fibre Toxicol. 7, 5. https://doi.org/10.1186/1743-8977-7-5.
Fairley, N., Fernandez, V., Richard-Plouet, M., et al., 2021. Systematic and collaborative approach to problem solving using X-ray photoelectron spectroscopy. Appl. Surf. Sci. Adv. 5, 100112. https://doi.org/10.1016/j.apsadv.2021.100112.
Fantauzzi, M., Pacella, A., Atzei, D., Gianfagna, A., Andreozzi, G.B., Rossi, A., 2010. Combined use of X-ray photoelectron and mössbauer spectroscopic techniques in the analytical characterization of iron oxidation state in amphibole asbestos. Anal. Bioanal. Chem. 396, 2889–2898. https://doi.org/10.1007/s00216-010-3576-0.
Fischbacher, A., von Sonntag, C., Schmidt, T.C., 2017. Hydroxyl radical yields in the Fenton process under various pH, ligand concentrations and hydrogen peroxide/Fe (II) ratios. Chemosphere 182, 738–744. https://doi.org/10.1016/j.chemosphere.2017.05.039.
Fitzgerald, S.M., Harty, E.A., 2014. Antigorite: is it the forgotten asbestos? Prof. Saf. 59, 43–48.
Fubini, B., Areán, C.O., 1999. Chemical aspects of the toxicity of inhaled mineral dusts. Chem. Soc. Rev. 28, 373–381. https://doi.org/10.1039/A805639K.
Fubini, B., Mollo, L., 1995. Role of iron in the reactivity of mineral fibers. Toxicol. Lett. 82–83, 951–960. https://doi.org/10.1016/0378-4274(95)03531-1.
Gautier, J.-M., Oelkers, E.H., Schott, J., 2001. Are quartz dissolution rates proportional to B.E.T. surface areas? Geochem. Cosmochim. Acta 65, 1059–1070. https://doi.org/10.1016/S0016-7037(00)00570-6.
Gazzano, E., Petriglieri, J.R., Aldieri, E., Fubini, B., Laporte-Magoni, C., Pavan, C., Tomatis, M., Turci, F., 2023. Cytotoxicity of fibrous antigorite from New Caledonia. Environ. Res. 230, 115046. https://doi.org/10.1016/j.envres.2022.115046.
Ghio, A.J., Stewart, M., Sangani, R.G., Pavlisko, E.N., Roggli, V.L., 2023. Asbestos and iron. Int. J. Mol. Sci. 24, 12390. https://doi.org/10.3390/ijms241512390.
Gilmour, P.S., Brown, D.M., Beswick, P.H., MacNee, W., Rahman, I., Donaldson, K., 1997. Free radical activity of industrial fibers: role of iron in oxidative stress and activation of transcription factors. Environ. Health Perspect. 105 (Suppl. 5), 1313–1317. https://doi.org/10.1289/ehp.97105s51313.
Glusker, J.P., 1980. Citrate conformation and chelation: enzymic implications. Acc. Chem. Res. 13, 345–352. https://doi.org/10.1021/ar50154a002.
Golubev, S.V., Bénézeth, P., Schott, J., Dandurand, J.L., Castillo, A., 2009. Siderite dissolution kinetics in acidic aqueous solutions from 25 to 100 C and 0 to 50 atm pCO_2. Chem. Geol. 265, 13–19. https://doi.org/10.1016/j.chemgeo.2008.12.031.
Gualtieri, A.F., Bursi Gandolfi, N., Pollastri, S., Burghammer, M., Tibaldi, E., Belpoggi, F., Pollok, K., Langenhorst, F., Vigliaturo, R., Dražić, G., 2017a. New insights into the toxicity of mineral fibres: a combined in situ synchrotron μ-XRD and HR-TEM study of chrysotile, crocidolite, and erionite fibres found in the tissues of sprague-dawley rats. Toxicol. Lett. 274, 20–30. https://doi.org/10.1016/j.toxlet.2017.04.004.
Gualtieri, A.F., Lusvardi, G., Zoboli, A., Di Giuseppe, D., Lassinantti Gualtieri, M., 2019. Biodurability and release of metals during the dissolution of chrysotile, crocidolite and fibrous erionite. Environ. Res. 171, 550–557. https://doi.org/10.1016/j.envres.2019.01.011.
Gualtieri, A.F., Mossman, B.T., Roggli, V.L., 2017b. Towards a general model for predicting the toxicity and pathogenicity of mineral fibres. In: Gualtieri, A.F. (Ed.), Mineral Fibres: Crystal Chemistry, Chemical-Physical Properties, Biological Interaction and Toxicity, 18. EMU Notes Mineral, pp. 501–532. https://doi.org/10.1180/EMU-notes.18.15.
Gualtieri, A.F., Pollastri, S., Bursi Gandolfi, N., Gualtieri, M.L., 2018. In vitro acellular dissolution of mineral fibres: a comparative study. Sci. Rep. 8, 7071. https://doi.org/10.1038/s41598-018-25531-4.
Gulumian, M., Kilroe Smith, T.A., de Jager, P., 2001. Lysosomal participation in the toxicity of mineral dusts. Environ. Health Perspect. 109 (Suppl. 4), 703–706. https://doi.org/10.1289/ehp.01109s4703.
Haber, F., Weiss, J., 1934. The catalytic decomposition of hydrogen peroxide by iron salts. Proc. R. Soc. Lond. A Math. Phys. Sci. 147, 332–351. https://doi.org/10.1098/rspa.1934.0221.
Horcas, I., Fernández, R., Gómez-Rodríguez, J.M., Colchero, J., Gómez-Herrero, J., Baro, A.M., 2007. WSXM: a software for scanning probe microscopy and a tool for nanotechnology. Rev. Sci. Instrum. 78, 013705. https://doi.org/10.1063/1.2432410.
ICDD, 2021. Powder Diffraction File (PDF-2, Release 2021). International Centre for Diffraction Data, Newtown Square, Pennsylvania, USA.
Innes, E., Yiu, H.H.P., McLean, P., Brown, W., Boyles, M., 2021. Simulated biological fluids – a systematic review of their biological relevance and use in relation to inhalation toxicology of particles and fibres. Crit. Rev. Toxicol. 51, 217–248. https://doi.org/10.1080/10408444.2021.1903386.
Kilaas, R., 1998. Optimal and near-optimal filters in high-resolution electron microscopy. J. Microsc. 190, 45–51. https://doi.org/10.1046/j.1365-2818.1998.3070861.x.
Königsberger, L.C., Königsberger, E., May, P.M., Hefter, G.T., 2000. Complexation of iron (III) and iron(II) by citrate. Implications for iron speciation in blood plasma. J. Inorg. Biochem. 78, 175–184. https://doi.org/10.1016/s0162-0134(99)00222-6.
Lacinska, A.M., Styles, M.T., Bateman, K., Wagner, D., Hall, M.R., Gowing, C., Brown, P. D., 2016. Acid-dissolution of antigorite, chrysotile and lizardite for *ex situ* carbon capture and storage by mineralisation. Chem. Geol. 437, 153–169. https://doi.org/10.1016/j.chemgeo.2016.05.015.
Lasaga, A.C., Lüttge, A., 2003. A model for crystal dissolution. Eur. J. Mineral 15, 603–615. https://doi.org/10.1127/0935-1221/2003/0015-0603.
Lüttge, A., Arvidson, R.S., Fischer, C., 2013. A stochastic treatment of crystal dissolution kinetics. Elements 9, 183–188. https://doi.org/10.2113/gselements.9.3.183.
Mellini, M., 1982. The crystal structure of lizardite 1T: hydrogen bonds and polytypism. Am. Mineral. 67, 587–598.
Nagai, H., Ishihara, T., Lee, W.-H., Ohara, H., Okazaki, Y., Okawa, K., Toyokuni, S., 2011. Asbestos surface provides a niche for oxidative modification. Cancer Sci. 102, 2118–2125. https://doi.org/10.1111/j.1349-7006.2011.02087.x.
Oze, C., Solt, K., 2010. Biodurability of chrysotile and tremolite asbestos in simulated lung and gastric fluids. Am. Mineral. 95, 825–831. https://doi.org/10.2138/am.2010.3265.
Pacella, A., Andreozzi, G., Nodari, L., Ballirano, P., 2019. Chemical and structural characterization of UICC crocidolite fibres from Koegas Mine, Northern Cape (South Africa). Period. Minerals 88, 297–306. https://doi.org/10.2451/2019PM910.
Pacella, A., Andreozzi, G.B., Corazzari, I., Tomatis, M., Turci, F., 2018. Surface reactivity of amphibole asbestos: a comparison between two tremolite samples with different surface area. Period. Minerals 87, 195–205. https://doi.org/10.2451/2018PM791.
Pacella, A., Ballirano, P., Di Carlo, M.C., Altieri, A., Paccapelo, M., Skogby, H., Campopiano, A., Bruno, M.R., Croce, A., Piersante, C., Apollaro, C., Malvasi, G., Bruni, B.M., Bloise, A., 2024. Geological and mineralogical characterization of fibrous tremolite from Iacolinei quarry (Basilicata, Italy). Environ. Geochem. Health 46, 429. https://doi.org/10.1007/s10653-024-02196-9.
Pacella, A., Ballirano, P., Di Carlo, M.C., Fantauzzi, M., Rossi, A., Nardi, E., Viti, C., Arrizza, L., Campopiano, A., Cannizzaro, A., Bloise, A., Montereali, M.R., 2023. Dissolution reaction and surface modification of UICC amosite in mimicked Gamble's solution: a step towards filling the gap between asbestos toxicity and its crystal chemical features. Nanomaterials 13, 2933. https://doi.org/10.3390/nano13222933.
Pacella, A., Ballirano, P., Fantauzzi, M., Rossi, A., Nardi, E., Capitani, G., Arrizza, L., Montereali, M.R., 2021. Surface and bulk modifications of amphibole asbestos in mimicked Gamble's solution at acidic pH. Sci. Rep. 11, 14249. https://doi.org/10.1038/s41598-021-93758-9.
Pacella, A., Tomatis, M., Viti, C., Bloise, A., Arrizza, L., Ballirano, P., Turci, F., 2020. Thermal inertization of amphibole asbestos modulates Fe topochemistry and surface reactivity. J. Hazard Mater. 398, 123119. https://doi.org/10.1016/j.jhazmat.2020.123119.
Petriglieri, J.R., Barale, L., Viti, C., Ballirano, P., Belluso, E., Bruno, M.R., Campopiano, A., Cannizzaro, A., Fantauzzi, M., Gianchiglia, F., Montereali, M.R., Nardi, E., Olori, A., Piana, F., Tomatis, M., Rossi, A., Skogby, H., Pacella, A., Turci, F., 2023. From field analysis to nanostructural investigation: a multidisciplinary approach to describe natural occurrence of asbestos in view of hazard assessment. J. Hazard Mater. 457, 131754. https://doi.org/10.1016/j.jhazmat.2023.131754.
Petriglieri, J.R., Capitani, G., Ballirano, P., Barale, L., Piana, F., Tomatis, M., Di Carlo, M. C., Gianchiglia, F., Campopiano, A., Olori, A., Bruno, M.R., Montereali, M.R., Nardi, E., Fantauzzi, M., Rossi, A., Skogby, H., Belluso, E., Turci, F., Pacella, A., 2025. Naturally occurring asbestos in Southern Italy: geological and mineralogical investigation of fibrous antigorite from Calabrian serpentinites in view of its hazard assessment. Sci. Total Environ. 970, 178970. https://doi.org/10.1016/j.scitotenv.2025.178970.
Pokrovsky, O.S., Golubev, S.V., Schott, J., Castillo, A., 2009. Calcite, dolomite and magnesite dissolution kinetics in aqueous solutions at acid to circumneutral pH, 25 to 150 °C and 1 to 55 atm *p*CO2: new constraints on CO2 sequestration in sedimentary basins. Chem. Geol. 265, 20–32. https://doi.org/10.1016/j.chemgeo.2009.01.013.
Pollastri, S., Gualtieri, A.F., Vigliaturo, R., Ignatyev, K., Strafella, E., Pugnaloni, A., Croce, A., 2016. Stability of mineral fibres in contact with human cell cultures. An in situ μXANES, μXRD and XRF iron mapping study. Chemosphere 164, 547–557. https://doi.org/10.1016/j.chemosphere.2016.08.139.
Reilman, R.F., Msezane, A., Manson, S.T., 1976. Relative intensities in photoelectron spectroscopy of atoms and molecules. J. Electron. Spectrosc. Relat. Phenom. 8, 389–394. https://doi.org/10.1016/0368-2048(76)80025-4.
Schott, J., Berner, R.A., 1983. X-ray photoelectron studies of the mechanism of iron silicate dissolution during weathering. Geochem. Cosmochim. Acta 47, 2233–2240. https://doi.org/10.1016/0016-7037(83)90046-7.
Scofield, J.H., 1976. Hartree-Slater subshell photoionization cross-sections at 1254 and 1487 eV. J. Electron. Spectrosc. Relat. Phenom. 8, 129–137. https://doi.org/10.1016/0368-2048(76)80015-1.
Seah, M.P., Dench, W.A., 1979. Quantitative electron spectroscopy of surfaces: a standard data base for electron inelastic mean free paths in solids. Surf. Interface Anal. 1, 2–11. https://doi.org/10.1002/sia.740010103.
Shukla, A., Gulumian, M., Hei, T.K., Kamp, D., Rahman, Q., Mossman, B.T., 2003. Multiple roles of oxidants in the pathogenesis of asbestos-induced diseases. Free Radic. Biol. Med. 34, 1117–1129. https://doi.org/10.1016/S0891-5849(03)00060-1.
Siever, R., Woodford, N., 1979. Dissolution kinetics and the weathering of mafic minerals. Geochem. Cosmochim. Acta 43, 717–724. https://doi.org/10.1016/0016-7037(79)90255-2.

Someah, M.S., Golbabaei, F., Arjomandi, R., Semiromi, F.B., Mohammadi, A., 2023. Oxidative stress and DNA damages induced by occupational exposure to asbestos: a systematic review. Iran. J. Public Health 52, 1613–1625. https://doi.org/10.18502/ijph.v52i8.13400.

Turci, F., Tomatis, M., Lesci, I.G., Roveri, N., Fubini, B., 2011. The iron-related molecular toxicity mechanism of synthetic asbestos nanofibres: a model study for high-aspect-ratio nanoparticles. Chem. Eur J. 17, 350–358. https://doi.org/10.1002/chem.201001893.

Van Oss, C.J., Naim, J.O., Costanzo, P.M., Giese Jr., R.F., Wu, W., Sorling, A.F., 1999. Impact of different asbestos species and other mineral particles on pulmonary pathogenesis. Clays Clay Miner. 47, 697–707. https://doi.org/10.1346/CCMN.1999.0470603.

Wagner, J.C., Berry, G., Skidmore, J.W., Timbrell, V., 1982. The effects of the inhalation of asbestos in rats. Br. J. Cancer 45, 124–135. https://doi.org/10.1038/bjc.1982.15.

WHO, 1997. Determination of airborne fibre number concentrations. A recommended method, by phase-contrast optical microscopy (membrane filter method) [WWW Document]. URL. https://www.who.int/publications/i/item/9241544961, 8.6.25.

Winterbourn, C.C., 1995. Toxicity of iron and hydrogen peroxide: the Fenton reaction. Toxicol. Lett. 82–83, 969–974. https://doi.org/10.1016/0378-4274(95)03532-X.

Wood, S.A., Taunton, A.E., Normand, C., Gunter, M.E., 2006. Mineral-fluid interaction in the lungs: insights from reaction-path modeling. Inhal. Toxicol. 18, 975–984.